The Astrophysical Journal, 953:142 (16pp), 2023 August 20 https://doi.org/10.3847/1538-4357/ace1e5

The Seoul National University AGN Monitoring Project. IV. Hα Reverberation Mapping of Six AGNs and the Hα Size–Luminosity Relation

Hojin Cho[1], Jong-Hak Woo[1], Shu Wang[1], Donghoon Son[1], Jaejin Shin[1,2,3], Suvendu Rakshit[1,4], Aaron J. Barth[5], Vardha N. Bennert[6], Elena Gallo[7], Edmund Hodges-Kluck[8,7], Tommaso Treu[9], Hyun-Jin Bae[1,10], Wanjin Cho[1], Adi Foord[11], Jaehyuk Geum[2], Yashashree Jadhav[1], Yiseul Jeon[1], Kyle M. Kabasares[5], Daeun Kang[1], Wonseok Kang[12,13], Changseok Kim[1], Donghwa Kim[1,14], Minjin Kim[2], Taewoo Kim[12,15,13], Huynh Anh N. Le[1,16], Matthew A. Malkan[9], Amit Kumar Mandal[1], Daeseong Park[3,2], Songyoun Park[1], Hyun-il Sung[3], Vivian U[5], and Peter R. Williams[9]
[1] Department of Physics & Astronomy, Seoul National University, Seoul 08826, Republic of Korea; woo@astro.snu.ac.kr
[2] Major in Astronomy and Atmospheric Sciences, Kyungpook National University, Daegu 41566, Republic of Korea
[3] Korea Astronomy and Space Science Institute, Daejeon 34055, Republic of Korea
[4] Aryabhatta Research Institute of Observational Sciences, Manora Peak, Nainital-263001, Uttarakhand, India
[5] Department of Physics and Astronomy, 4129 Frederick Reines Hall, University of California, Irvine, CA 92697-4575, USA
[6] Physics Department, California Polytechnic State University, San Luis Obispo, CA 93407, USA
[7] Department of Astronomy, University of Michigan, Ann Arbor, MI 48109, USA
[8] NASA/GSFC, Code 662, Greenbelt, MD 20771, USA
[9] Department of Physics and Astronomy, University of California, Los Angeles, CA 90095-1547, USA
[10] Department of Astronomy, Yonsei University, Seoul 03722, Republic of Korea
[11] Kavli Institute of Particle Astrophysics and Cosmology, Stanford University, Stanford, CA 94305, USA
[12] National Youth Space Center, Goheung 59567, Republic of Korea
[13] Spacebeam Inc., Cheongju 28165, Republic of Korea
[14] Graduate School of Data Science, Seoul National University, Seoul 08826, Republic of Korea
[15] Department of Astronomy and Space Science, Chungbuk National University, Cheongju 28644, Republic of Korea
[16] CAS Key Laboratory for Research in Galaxies and Cosmology, Department of Astronomy, University of Science and Technology of China, Hefei 230026, People's Republic of China
Received 2023 March 30; revised 2023 June 12; accepted 2023 June 25; published 2023 August 11

Abstract

The broad-line region (BLR) size–luminosity relation has paramount importance for estimating the mass of black holes in active galactic nuclei (AGNs). Traditionally, the size of the Hβ BLR is often estimated from the optical continuum luminosity at 5100 Å, while the size of the Hα BLR and its correlation with the luminosity is much less constrained. As a part of the Seoul National University AGN Monitoring Project, which provides 6 yr photometric and spectroscopic monitoring data, we present our measurements of the Hα lags of high-luminosity AGNs. Combined with the measurements for 42 AGNs from the literature, we derive the size–luminosity relations of the Hα BLR against the broad Hα and 5100 Å continuum luminosities. We find the slope of the relations to be 0.61 ± 0.04 and 0.59 ± 0.04, respectively, which are consistent with the Hβ size–luminosity relation. Moreover, we find a linear relation between the 5100 Å continuum luminosity and the broad Hα luminosity across 7 orders of magnitude. Using these results, we propose a new virial mass estimator based on the Hα broad emission line, finding that the previous mass estimates based on scaling relations in the literature are overestimated by up to 0.7 dex at masses lower than $10^7\,M_\odot$.

Unified Astronomy Thesaurus concepts: Active galactic nuclei (16); Reverberation mapping (2019)

1. Introduction

Mass is the most important physical property of a black hole that we can measure. While the mass of a black hole can be determined by measuring its gravitational radius, this method thus far has been applied to only two black holes (Event Horizon Telescope Collaboration et al. 2019, 2022). For most extragalactic black holes, the mass is instead measured by observing the kinematics of orbiting bodies near the black hole. While the mass of several black holes has been measured via the kinematics of surrounding gas (e.g., Scharwächter et al. 2013; den Brok et al. 2015; Gravity Collaboration et al. 2018; Kabasares et al. 2022) or stars (e.g., van der Marel 1994; Nguyen et al. 2018, 2019), this technique requires an exceptional angular resolution that can resolve the sphere of influence of the black hole (Peebles 1972).

The mass of active galactic nuclei (AGNs) can be measured without good spatial resolution via reverberation mapping (Blandford & McKee 1982). By measuring the time delay (τ) of the broad emission line flux against the continuum, combined with its line width (ΔV) measured from the spectrum, the mass of the black hole ($M_\bullet$) can be determined using

$$M_\bullet = f\frac{c\,\tau\cdot\Delta V^2}{G} \quad (1)$$

where c is the vacuum speed of light and G is the gravitational constant. The virial factor, f, is a dimensionless scale factor reflecting the geometry and kinematics of the broad-line region (BLR). To date, the masses of more than 100 AGNs have been measured by applying this technique to broad Hβ lines (e.g., Bentz & Katz 2015).

This method can be extended to a far larger number of black holes using the size–luminosity relation of the Hβ-emitting zone of the BLR by estimating the time lag from the 5100 Å luminosity of the AGN accretion disk (e.g., Kaspi et al. 2000; Bentz et al. 2013). It provides a shortcut to estimating the broad-line time lag without going through a reverberation mapping campaign, offering a way to estimate the mass of the black hole with a single spectroscopic observation; hence, it is called the single-epoch method.

Compared to Hβ, the Hα-emitting zone of the BLR has been relatively unexplored, with Hα lag measurements of only ∼50 AGNs so far (e.g., Kaspi et al. 2000; Bentz et al. 2010; Grier et al. 2017). This is because observing Hα poses more challenges than observing Hβ. For instance, Hα is in the redder part of the optical spectrum, making it vulnerable to airglow lines as well as to Fraunhofer A and B band telluric absorption lines, given appropriate redshifts. Moreover, there is no strong narrow line in the vicinity of Hα that could be used for flux calibration, whereas the calibration of Hβ emission lines can utilize the invariant and strong fluxes of [O III] narrow lines.

Nevertheless, the benefit of using broad Hα lines for the single-epoch method outweighs its difficulty. First, measuring Hα flux is more reliable than measuring Hβ. The Hα line is stronger than the Hβ line by at least a factor of 3, and this factor increases to 4–6 for broad emission lines (Netzer 1990). Some AGNs even exhibit a relatively weak, if present at all, broad Hβ emission (Osterbrock 1981).

Furthermore, broad-line fluxes of Hα , as well as of Hβ, can be measured with less degeneracy than the continuum luminosity, making them an ideal proxy for the size–luminosity relation. The observed continuum luminosity in the AGN spectrum is contaminated by starlight from the host galaxy or synchrotron radiation from the jet in the case of radio-loud AGNs, which must be removed to use the relation. The removal of host stellar emission can be achieved either by modeling the image of the AGN to determine the host galaxy fraction to the AGN spectrum with high-resolution images (e.g., Bentz et al. 2013) or by decomposing the continuum spectrum as a sum of the stellar and AGN components in the high signal-to-noise ratio (S/N) spectra (e.g., Park et al. 2012). The removal of jet contamination would require multiwavelength observations (e.g., Paltani et al. 1998; Soldi et al. 2008). Broad Hα/Hβ lines, on the other hand, are purely from the BLR of the AGN and can be separated from narrow lines.

There is, however, one difficulty in using Hα for single-epoch mass estimation: a size–luminosity relation involving Hα luminosity has not yet been reported. As a workaround, Greene & Ho (2005) demonstrated an empirical relation between the broad Hα line luminosity and the 5100 Å continuum luminosity and proposed to use it in conjunction with the Hβ size–luminosity relation to construct an Hα-based single-epoch mass estimator. To date, it has been applied to a number of AGNs that are too faint for researchers to measure the AGN 5100 Å luminosity and/or Hβ line width correctly. In particular, the masses of low-luminosity AGNs and active intermediate-mass black holes (IMBHs) have been measured using this recipe (e.g., Reines et al. 2013; Shin et al. 2022), which suffers from substantial uncertainty due to the scatter of the scaling relations. Therefore, a relation between the size of the Hα BLR and the broad Hα luminosity will provide more robust estimations.

The Seoul National University AGN Monitoring Project (SAMP; Rakshit et al. 2019; Woo et al. 2019b) is a reverberation mapping campaign aimed at the Hβ time lags of dozens of high-luminosity AGNs to expand the size–luminosity relation toward a higher-luminosity regime. In this paper, we present the SAMP results on Hα time lag measurements and demonstrate a new empirical relation between the Hα BLR size and the broad Hα luminosity. In Section 2, we describe the data acquisition and reduction. In Section 3, we perform spectral decomposition and Hα flux measurements. The time lag measurements are provided in Section 4. Section 5 presents the size–luminosity relation of the Hα broad line. We discuss the implications of this size–luminosity relation in Section 6. Section 7 gives a brief summary of the paper. Throughout this paper, we adopt a flat ΛCDM cosmology with $H_0 = 72\ \mathrm{km\ s^{-1}\ Mpc^{-1}}$ and $\Omega_\mathrm{m} = 0.3$.

2. Observations and Data Reduction

The initial sample of SAMP observations consisted of 100 AGNs selected from the literature, described in detail by Woo et al. (2019b). To briefly summarize, 85 AGNs in the local Universe ($z < 0.5$) with $V < 17$ were selected from the Million Quasars Catalog (MILLIQUAS; Flesch 2015, 2021), whose observed-frame lags were expected to be $40 < (1+z)\tau_{\mathrm{H}\beta} < 250$ days based on the *R–L* relation of Bentz et al. (2013). The other 15 AGNs were selected from the Palomar-Green catalog (Boroson & Green 1992). During the first few years, we were able to identify AGNs with very low variability. Note that since the expected lag of the sample is relatively long, we were able to predict whether the line flux would vary at each epoch based on the photometric light curves. By selecting the most variable sources, we narrowed down the sample to 32 objects for continuous monitoring for 6 yr, by excluding objects with weak variability. In this paper, we specifically focus on 13 objects of which the Hα lines were observable with our spectral configurations.

2.1. Photometry

We carried out our photometric monitoring observations using several telescopes, including the MDM 1.3 and 2.4 m telescopes, the Lemmonsan Optical Astronomy Observatory (LOAO) 1 m telescope, the Lick Observatory 1 m nickel telescope, the Las Cumbres Observatory Global Telescope (LCOGT) network, and the Deokheung Optical Astronomy Observatory (DOAO) 1 m telescope. The acquisition of photometric images, reduction processes, and photometry are described in our previous paper (J.-H. Woo et al. 2023, in preparation). Here, we use fully reduced and intercalibrated *B*- and *V*-band light curves. Typically, the *B*-band light curves spanned ∼2000 days with a median cadence of 4 days, resulting in ∼250 epochs, except for Mrk 1501, which was observed for 115 epochs over 1740 days with a median cadence of 6 days. The *V*-band light curves were acquired with a median cadence of 1 week.

2.2. Spectroscopy

Spectroscopic observations of Hα lines were carried out using the Shane 3 m telescope, located at the Lick Observatory on Mount Hamilton, California, USA. Note that while we used the Lick 3 m and MDM 2.4 m telescopes for SAMP, we only used the Lick 3 m data, which covers the Hα line. The details

of the spectroscopic observations of SAMP were described by Rakshit et al. (2019).

We used the Kast Double Spectrograph,[17] which employs dichroic beam splitters to acquire the red-side and blue-side spectra simultaneously. We used the red-side spectra with a 600 line mm^{-1} grating. At the beginning of the campaign, the wavelength coverage of our spectra was 4450–7280 Å with 2.33 Å $pixel^{-1}$ sampling, and the spectra obtained during this period are hereafter denoted as the *early-configuration spectra*. In 2016 September, the detector was replaced with a 2K × 4K CCD, covering 4750–8120 Å with 1.27 Å $pixel^{-1}$ sampling, and the wavelength coverage was slightly adjusted to 5050–8424 Å in 2019 March. Spectra obtained after 2016 September are hereafter denoted as *late-configuration spectra*, which constitute 80% of the epochs. We used a 4″ slit width to minimize slit loss. The instrumental resolving power is $R = 650$, which was measured from unblended airglow lines near 7500 Å. This corresponds to the FWHM velocity of 460 km s^{-1}. Note that the actual resolution of AGN spectra would be better than what is measured from night sky emissions since the slit width is larger than the seeing FWHM (1.″5–4″).

Each night, we obtained the bias, arc, and flat frames at the beginning and end of the night. Note that the arc lamp images were taken using a 0.″5 width slit to improve the accuracy of the wavelength solution. We also observed at least one of the spectrophotometric standard stars listed by Oke (1990), and any spectra taken on nights without spectrophotometric stars were discarded from the Hα analysis.

The red-side spectra of Lick/Kast were preprocessed primarily using `PypeIt` v1.4 (Prochaska et al. 2020a, 2020b). This pipeline was chosen to minimize human intervention in the fitting of the wavelength solution and the sensitivity function. The latter is particularly susceptible to human factors due to the highly variable telluric OH absorption band near the red-side edge of the spectra. We created pixel flats and traced the slit using dome flat-field images. The wavelength solutions were derived using Ne and Ar lines in the arc frames in full template mode, and barycentric corrections were applied to each object frame. We used the optimal extraction algorithm (Horne 1986), implemented in `PypeIt`, to obtain photon-count spectra because optimally extracted spectra yield higher S/N than those produced with standard aperture extraction. The optimal extraction algorithm is generally not recommended for extended objects such as AGNs with resolved narrow-line regions (e.g., Barth et al. 2015). However, we confirm that all objects in our campaign did not show extended narrow lines, even under the best seeing conditions (typically $\leqslant$1.″5). Furthermore, the resulting optimally extracted spectra showed no differences from the aperture-extracted spectra, except for having a higher S/N.

2.2.1. Flux Calibration

We visually inspected all spectra of the spectrophotometric standard stars. After masking strong Balmer absorption lines, sensitivity functions were constructed from each reliable standard star spectrum by jointly fitting it with polynomial functions of the wavelength and a model of telluric absorption lines using a script provided by `PypeIt` in IR mode. This yielded one to six different sensitivity functions per successful night. We derived the median value of the individual sensitivity function, and the function that showed the median sensitivity of a given night was chosen to be the representative sensitivity function of that night.

The spectra of the AGNs and standard stars were then calibrated using the representative sensitivity for that night. We discarded any spectra taken on nights that failed to produce at least one reliable sensitivity. Then, the atmospheric extinction was corrected based on the airmass difference between the sensitivity function and the object frame.

To further calibrate the flux in each spectrum, we compared the synthetic *V*-band flux obtained from the spectrum with the photometric light curves. First, we constructed a Javelin model (Zu et al. 2016) of the photometric *V*-band light curve and interpolated it onto each spectral epoch. The *B*-band light curve, which has a much shorter cadence, was jointly modeled with the *V*-band light curve to improve the quality of the interpolation. Then, each spectrum, after being multiplied by the *V*-band filter transmission curve, was integrated to synthesize the *V*-band flux. Finally, we scaled the spectra so that the synthetic *V*-band flux was the same as the photometric flux. Note that the *late-configuration spectra* did not cover the entirety of the *V*-band bandwidth. For these epochs, we calculated the portion of *V*-band flux that was included in each spectrum based on the *early-configuration spectra*, which was ∼80% on average, assuming that the spectral shape of the AGNs did not change significantly over the campaign period.

2.2.2. Telluric Correction

The telluric absorption features were corrected using a set of atmospheric absorption line models of the Lick Observatory provided by `PypeIt`. This consists of 28,413 high-spectral-resolution model spectra of telluric absorption lines. We first performed principal component analysis (PCA) on the models and chose the largest 25 components. Then, we fitted the calibrated spectra of the spectrophotometric standards with the PCA components using `pPXF` (Cappellari 2017) to obtain the weight for each component to reconstruct a high-resolution telluric model for each standard spectrum. We averaged the telluric models for each night to create the nightly telluric model spectrum. Then, for each object spectrum, we masked the narrow lines and fitted the red part ($\lambda_{obs} > 6500$ Å) with the nightly model and polynomial functions using `pPXF`. After shifting and broadening the model by the best-fit parameters provided by `pPXF`, we divided the spectrum by the model to generate a telluric-corrected spectrum of our targets. An example of the telluric correction is shown in Figure 1. After correcting for telluric absorption lines, the corrected flux level is consistent with the nearby continuum. However, we note strong residuals for a couple of spectra for each object after removing the telluric lines, which are presumably due to the decreased S/N. Nevertheless, these residual features did not affect our spectral analysis, as the residual features are far narrower than the AGN emission lines.

2.2.3. Shift Correction

Despite the wavelength calibration and the barycentric corrections, the wavelength solutions deviated between the different spectra by several angstroms because of instrumental flexure and/or pointing accuracy within the slit. To compensate for this, we shifted each spectrum so that the peak of the

[17] https://mthamilton.ucolick.org/techdocs/instruments/kast/

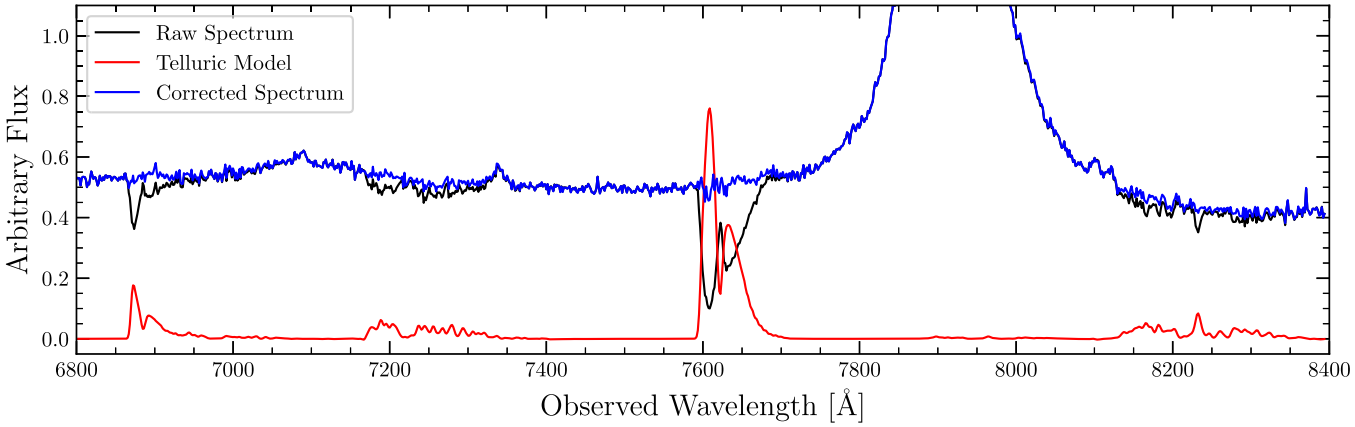

Figure 1. An example of the telluric correction. The black line represents the flux-calibrated spectrum of PG 0947+396 without telluric correction. Red represents the telluric model in the optical depth units (arbitrarily scaled), with the velocity and velocity dispersion adjusted to fit the AGN spectrum. Blue is the AGN spectrum after correcting for telluric absorption.

Table 1
Hα Objects

	Name (1)	SDSS Identifier (2)	R.A. (3)	Decl. (4)	z (5)	A_V (6)	N_{ph} (7)	Δt_{ph} (8)	N_{sp} (9)	Δt_{sp} (10)	SAMP ID (11)
1	Mrk 1501	J001031.00+105829.4	00:10:31.0	+10:58:29.5	0.0893	0.269	115	6	22	37	P02
2	J0101+422	J010131.17+422935.5	01:01:31.1	+42:29:36.0	0.1900	0.238	255	4	38	22	Pr1_ID01
3	PG 0947+396	J095048.39+392650.4	09:50:48.4	+39:26:50.5	0.2059	0.052	267	4	31	29	Pr1_ID15
4	J1217+333	J121752.16+333447.2	12:17:52.2	+33:34:47.3	0.1784	0.036	246	4	25	31	Pr1_ID29
5	VIII Zw 218	J125337.71+212618.2	12:53:37.7	+21:26:18.2	0.1274	0.135	239	4	38	29	Pr1_ID30
6	PG 1440+356	J144207.47+352622.9	14:42:07.5	+35:26:23.0	0.0791	0.038	235	4	34	29	Pr2_ID26

Note. The columns indicate (1) the object name, (2) the Sloan Digital Sky Survey (SDSS) identifier, (3) the R.A. (J2000), (4) the decl. (J2000), (5) the redshift (from NASA/IPAC Extragalactic Database (NED) 2019), (6) the galactic extinction in the V band by Schlafly & Finkbeiner (2011), (7) the number of epochs in the photometric light curve, (8) the median cadence of the photometric light curve, (9) the number of epochs in the spectroscopic light curve, (10) the median cadence of the spectroscopic light curve, and (11) the SAMP ID (refer to Woo et al. 2019b).

Hα line fell exactly on the theoretical wavelength of Hα. Note that the Hα line is easier to use for this purpose compared to much weaker narrow emission lines. We first calculated the derivatives of the individual spectra by applying a Savitzky–Golay filter using `SciPy` (Virtanen et al. 2020) with a window width of ∼1260 km s^{-1}, and the peak of Hα was calculated by finding the root of the derivatives. The window width was chosen based on experiments so that the secondary peaks due to [N II] lines were smoothed out. Finally, we shifted and resampled the spectra.

Among the full sample of 32 AGNs that were monitored, 13 objects showed Hα in the observed spectra, depending on the redshift. Four of them suffered from strong telluric absorption because the Fraunhofer A band fell on the very center of the Hα line. For these objects, the described telluric correction was unreliable, so we did not analyze them further. Additionally, there were fewer than 20 spectra available for three objects, which is unsuitable for time-series analysis. We discarded these objects as well. We present the analysis of the remaining six objects, whose properties are summarized in Table 1.

3. Spectral Analysis

Many of the early reverberation mapping studies measured the broad Hα line flux by directly integrating the spectrum within a fixed range without fitting the line profile with a model. In this case, the continuum below the emission line was fitted with a straight line at the two ends of the Hα line profile (e.g., Kaspi et al. 2000; Bentz et al. 2010). While this procedure is straightforward, we found it insufficient for our objects at higher redshift. First, the Hα emission line of our objects is located close to the edge of the detector, making it challenging to directly determine the continuum level. This is further complicated by the presence of telluric OH absorption lines near the edge of the detector. Although the absorption was averaged out through correction, some epochs exhibited strong residuals due to velocity mismatch. Finally, some of our AGNs displayed moderate Fe II lines in the blue-side continuum of Hα. While their fluxes were relatively small compared to the continuum or Hα emission, they were still strong enough to influence the slope of the continuum fit, thereby reducing the accuracy of the Hα flux. This issue is similar to what was pointed out by Barth et al. (2015) regarding the construction of Hβ light curves. It is therefore preferable to model the line profiles and measure the broad Hα flux at each epoch.

To do this, we first constructed the mean spectrum for each object. We modeled its continuum as a power law along with the Fe II lines based on the model by Boroson & Green (1992) using suitable windows, i.e., 4175–4250 Å, 4500–4725 Å, 5090–5780 Å, 6000–6280 Å, and 6800–7650 Å, in the rest frame, if covered by the spectrograph. Portions of the spectrum that showed either (1) strong telluric residuals or (2) strong narrow lines were masked before the continuum fitting, leaving at least one window on the blue side of Hβ, one between Hα and Hβ, and one on the red side of Hα. We did not include the stellar host continuum in the model since our six objects do not exhibit strong stellar absorption features. We determined

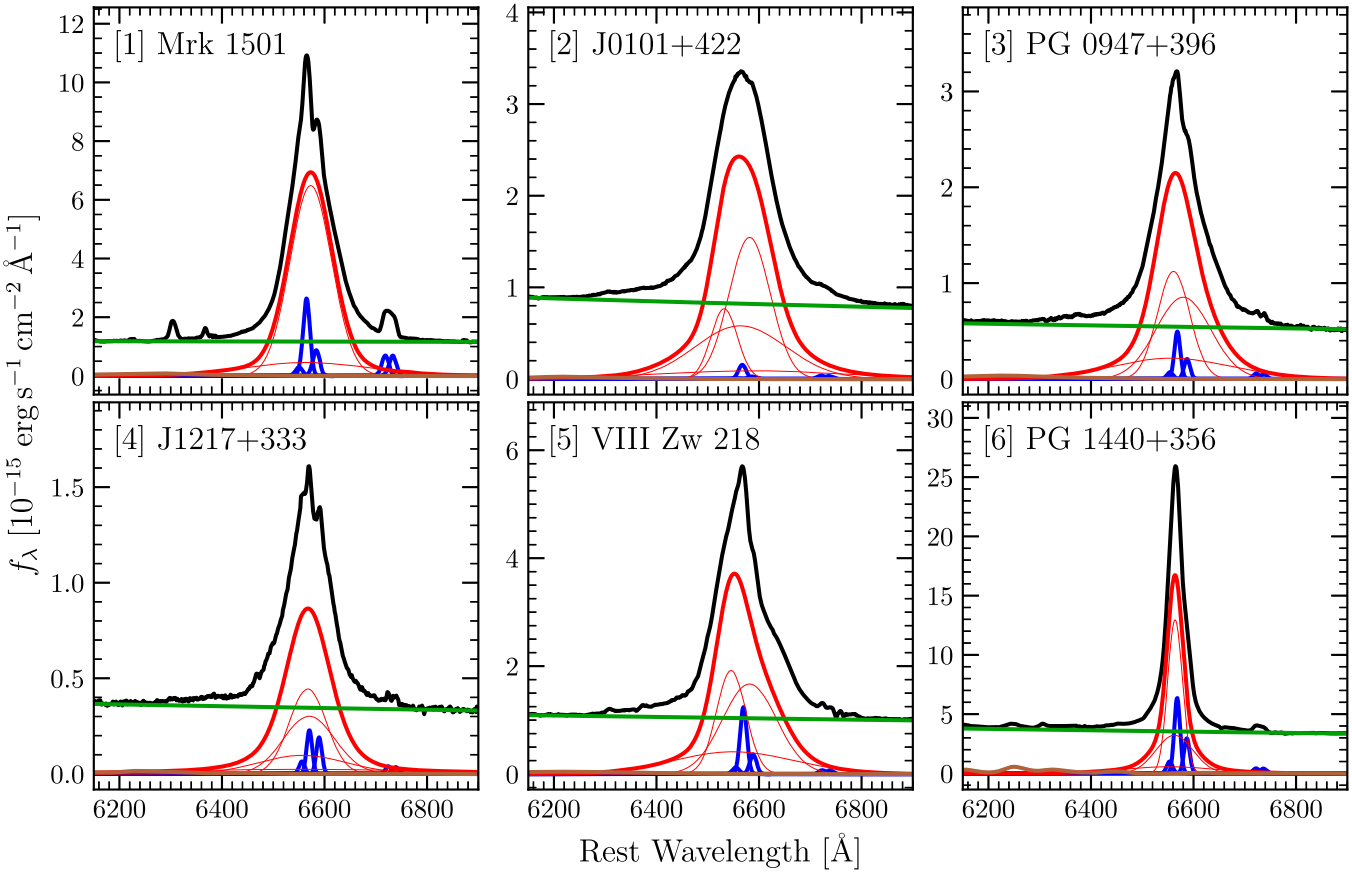

Figure 2. Mean spectra of six objects around the Hα line and their best-fit models. Black represents the mean spectrum, green represents the power-law continuum, and brown represents the Fe II model from Boroson & Green (1992). Each blue line represents a narrow emission line. The thick red line shows the broad Hα model, whereas the thin red lines show the individual Gaussian components of the model.

the best-fit model based on the maximum likelihood method using the `zeus` Markov Chain Monte Carlo (MCMC) sampler (Karamanis & Beutler 2020; Karamanis et al. 2021). The best-fit models of the continuum and Fe II lines were subtracted from the mean spectrum, leaving the line spectrum only.

To constrain the narrow-line profile, we first modeled the [S II] λλ6717, 6731 doublet. First, we fitted the wing of the broad Hα as a cubic polynomial in the windows of 6685–6708 Å and 6760–6785 Å. After subtracting the model of the broad Hα wing, each of the [S II] lines was fitted with a single Gaussian profile using the maximum likelihood estimators. The acquired models of the [S II] were then subtracted from the observed spectrum. Then, the narrow Hα and [N II] lines were modeled as one to two Gaussian profiles, with shared shifts and widths among different lines, along with a sum of two to four independent Gaussian profiles for broad Hα. Upon fitting, we masked the [O I] λλ6300, 6364 lines and, in the case of VIII Zw 218, the telluric line residuals as well. We imposed a prior such that the narrow-line shifts and widths followed normal distributions centered at the measurement from [S II] with a standard deviation of ∼100 km s^{-1}. Furthermore, we restricted the parameters to the following bounds: (1) the velocity shift of any component is within ±1600 km s^{-1}, (2) the narrow-line dispersion is smaller than 800 km s^{-1}, and (3) the line dispersion of any Gaussian in the broad-line model is smaller than 30,000 km s^{-1}, and it was further restricted based on visual inspection of the spectrum. We adopted the maximum a posteriori estimator from MCMC samplings as our mean spectrum model. We also measured the FWHMs of the model line profiles and found their uncertainties based on Monte Carlo randomization for 1000 iterations. At each iteration, we added Gaussian random noise to the model parameters based on their measurement uncertainties and constructed a randomized profile. We measured the FWHMs of the randomized profiles and adopted their standard deviation as the uncertainty of the FWHM. The decomposed Hα and other narrow lines are shown in Figure 2, and the measurements after subtraction of the instrumental resolving power, $R = 650$, are summarized in Table 2. Note that the line widths listed here should only be used as a reference to the fit quality since the resolving power measured from the airglow lines can be underestimated, as noted in Section 2.2.

To measure the broad Hα flux from each epoch, we modeled the spectra from individual nights using the mean spectrum model. We first modeled and subtracted the continuum and Fe II lines using the same wavelength windows. We masked the [O I] lines and telluric residuals as we did upon fitting the mean spectra. Then, assuming the narrow lines did not change over the period of observations, we subtracted the narrow-line model obtained from the mean spectrum. After subtracting the continuum, Fe II, and narrow lines, the residual spectrum contained the broad Hα line only. We constructed the prior for the multiple Gaussian models for broad Hα as follows. For the parameters that determined the shape of the Hα line (i.e., the flux ratio and first/second-moment differences between any pair of Gaussian components), we imposed Gaussian priors with the mean and the standard deviation from the mean spectrum model. We did not favor any specific value for the

Table 2
Line Width Measurements

	Object	Narrow			Broad Hα		
		N	σ (km s^{-1})	FWHM (km s^{-1})	N	σ (km s^{-1})	FWHM (km s^{-1})
	(1)	(2)	(3)	(4)	(5)	(6)	(7)
1	Mrk 1501	2	287 ± 159	542 ± 231	2	2845 ± 465	4532 ± 258
2	J0101+422	1	279 ± 207	657 ± 489	4	3862 ± 1295	5819 ± 1624
3	PG 0947+396	1	176 ± 207	415 ± 488	3	3173 ± 808	4553 ± 1099
4	J1217+333	1	146 ± 212	344 ± 500	4	4828 ± 4039	4762 ± 2040
5	VIII Zw 218	1	226 ± 187	532 ± 441	3	3322 ± 709	4788 ± 863
6	PG 1440+356	1	165 ± 186	388 ± 438	3	1896 ± 665	1741 ± 288

Notes. The columns indicate (1) the object name, (2) the number of Gaussian components in the narrow line, (3) the narrow-line width in σ, (4) the line width in FWHM, (5) the number of Gaussian components in the broad line, (6) the broad-line width in σ, and (7) the broad-line width in FWHM. All values presented here are those obtained after correcting for the instrumental resolution, $\mathrm{FWHM_{inst}} = 461$ km s^{-1} or $\sigma_{\mathrm{inst}} = 196$ km s^{-1}. The uncertainties shown here denote the standard deviation, where the uncertainty of σ was derived using the analytical model, and the uncertainty of FWHM was derived with 1000 iterations of Monte Carlo randomization (see Section 3).

Table 3
Rest-frame Hα Time Lag

	Object	ICCF (days)	zDCF (days)	Javelin (days)	Quality Rating
	(1)	(2)	(3)	(4)	(5)
1	Mrk 1501	67^{+24}_{-38}	42^{+44}_{-40}	148^{+6}_{-104}	B
2	J0101+422	118^{+17}_{-17}	82^{+34}_{-35}	95^{+1}_{-11}	A
3	PG 0947+396	71^{+16}_{-35}	30^{+83}_{-25}	120^{+1}_{-93}	B
4	J1217+333	201^{+143}_{-132}	39^{+432}_{-258}	-211^{+946}_{-284}	C
5	VIII Zw 218	140^{+26}_{-26}	102^{+92}_{-19}	139^{+33}_{-3}	A
6	PG 1440+356	80^{+63}_{-30}	62^{+68}_{-13}	61^{+3}_{-23}	A

Notes. The columns indicate (1) the object identifier, (2) the ICCF/CCCD lag, (3) the zDCF lag, (4) the Javelin lag, and (5) the quality rating as described in Section 4. The uncertainties shown here are the 68% central confidence intervals taken from the posterior distribution.

total flux of the Hα line and adopted a flat prior. For each spectrum, we calculated the maximum a posteriori estimators from MCMC samplings. Finally, the flux of the best-fit model was taken as the Hα flux of each epoch. Note that the uncertainty of the narrow emission line fitting did not affect the Hα lag measurements as we subtracted a constant flux of narrow emission lines in each epoch, which was expected to be nonvarying during the campaign.

4. Time Lag Measurements

We measured the time lags between the continuum and Hα line light curves using the interpolated cross-correlation function (ICCF; White & Peterson 1994) with a modified averaging scheme. We first converted the Hα line fluxes into magnitudes. After we calculated the continuum-interpolated ICCF and the line-interpolated ICCF, we took the Fisher transformation (Fisher 1921) on both one-sided ICCFs, averaged them, and then took the inverse transformation to obtain the z-transformed average ICCF. The ICCF centroid was calculated over the largest continuous interval containing the peak of the ICCF, where the ICCF values were larger than 80% of the peak value. We performed 10,000 realizations of flux randomization/random-subset selection (FR/RSS; Peterson et al. 1998, 2004). For each realization, we resampled each light curve and added random Gaussian noise to each flux value according to its measurement uncertainty. Duplicate points were averaged, and their uncertainties were divided by $\sqrt{n}$ to compensate for the duplication. The median of the distribution of the centroid and the central 68% confidence interval were taken as the time lag measurement and the associated uncertainties. To check the consistency with the ICCF, we also calculated the time lag using other commonly used methods, the z-transformed discrete correlation function (zDCF; Alexander 1997) and the Javelin model (Zu et al. 2011) Finally, we rated the quality of our lag measurements based on the lag differences among the different methods as follows:

1. Rating A if the ICCF lag, zDCF lag, and Javelin lag agree within 1σ and the maximum difference between them is within 2 months (60 days).
2. Rating B if the lag is measured (1σ above zero lag) with all three methods, while the maximum difference between them is larger than 2 months (60 days).
3. Rating C if the lag is not constrained or detected.

The measured lags are summarized in Table 3. The light curves and the cross-correlation functions (CCFs) of the individual objects are shown in Figures 3–8.

Here, we describe the individual measurements of the six targets. For Mrk 1501, we measured 68^{+23}_{-41} days of time lag. However, the CCFs at time lags between 100 days and 200 days were relatively unexplored due to the large seasonal gaps. This is reflected in the large difference of ICCFs when using different interpolation methods, as well as in the lack of points in the zDCF. The primary peak of the Javelin lag distribution falls within this seasonal gap, which raises questions about the accuracy of the Javelin lag for this specific case. We assess the lag of this object as rating B.

For J0101+422, we measured 117^{+17}_{-18} days of time lag. This is consistent with its zDCF and Javelin lags. We assess the lag of this object as rating A.

For PG 0947+396, we measured 71^{+16}_{-34} days of time lag. While this is consistent with the zDCF and Javelin lags, they both showed bimodality, where the zDCF preferred the smaller mode and Javelin preferred the larger mode. On the other hand, the ICCF lag captured the average between the two lags. We assess the lag of this object as rating B.

For J1217+333, our assessment is that our lag measurements are not reliable. Javelin is unconstrained, and the zDCF lag is consistent with 0 within its 68% confidence interval. While we

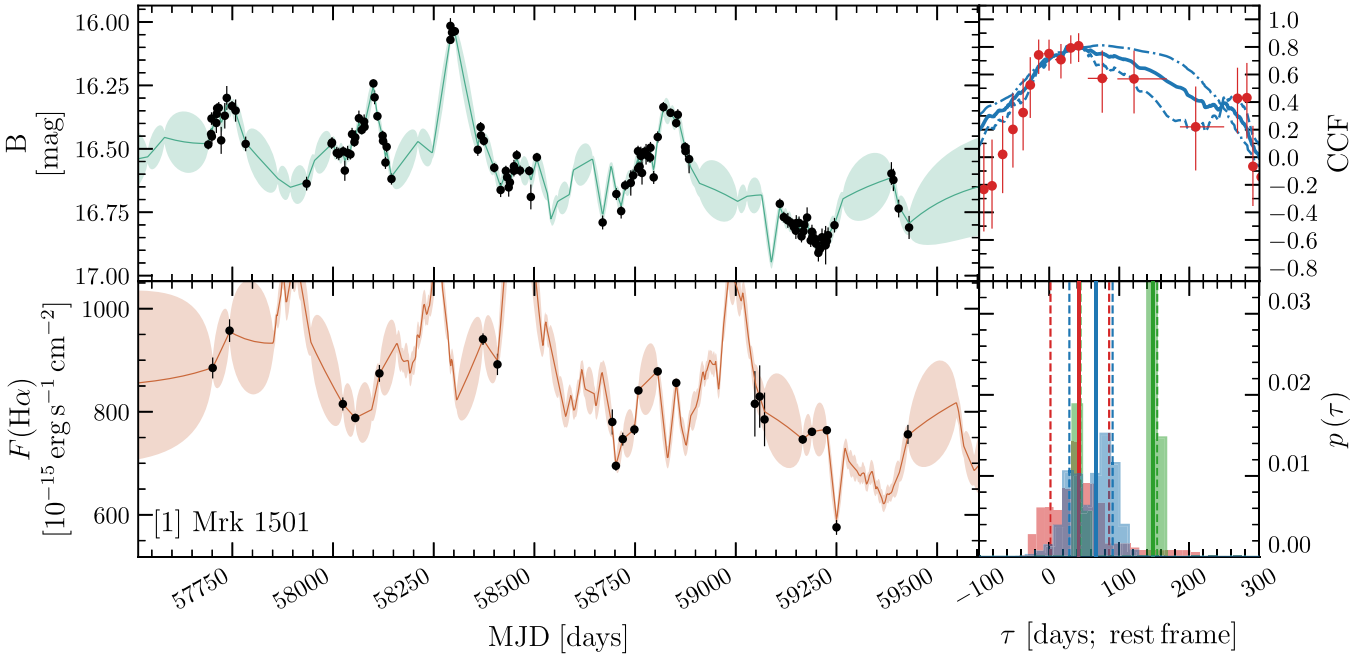

Figure 3. Light curves and time lag measurements of Mrk 1501. Upper left: *B*-band light curve, with the Javelin model and its uncertainty shown as a solid line and shaded region. Lower left: broad Hα light curve, with the Javelin model shown similarly. Upper right: blue lines indicate the ICCF, where the dashed line shows the ICCF upon interpolation of the continuum, and the dashed–dotted line shows the ICCF upon interpolation of the line flux. The solid line represents the *z*-transformed average between two interpolations, as described in Section 4. Red dots indicate the *z*DCF, where the horizontal error bars indicate the bin size of the *z*DCF, and the vertical error bars indicate the standard deviation within the bin. Lower right: the time lag measurements. The ICCF, *z*DCF, and Javelin are indicated by blue, red, and green colors, respectively. Vertical solid lines represent the median of each measurement, while dashed lines mark the 16th and 84th percentiles as 1σ uncertainties.

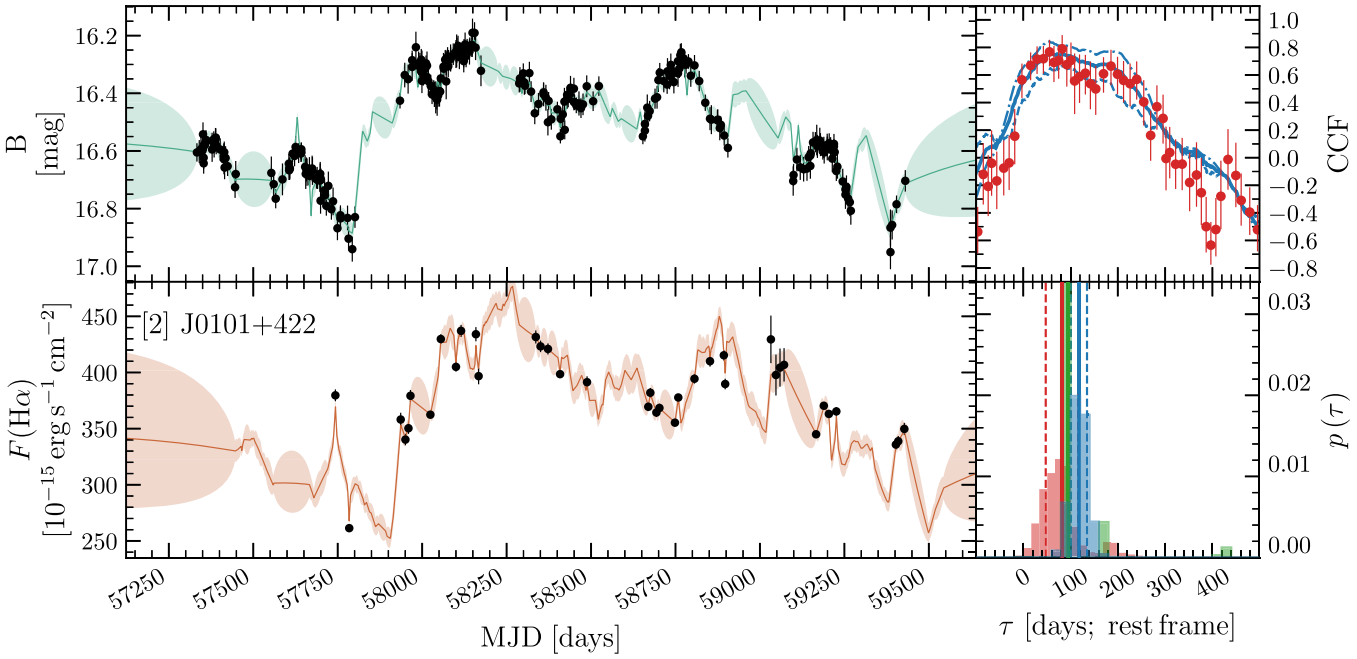

Figure 4. Light curves and time lag measurements of J0101+422. The panels are the same as those in Figure 3.

measured 199^{+137}_{-132} days from the ICCF, this is likely to be the average of the window size we used to find the lag. Supporting this, the ICCF and *z*DCF both showed multiple modes in the given window. Moreover, the value is far larger than what is measured using Hβ (J.-H. Woo et al. 2023, in preparation). We assess the lag of this object as rating C and exclude it from further analysis.

VIII Zw 218 showed a single, clean peak in CCFs, and we measured 140^{+25}_{-25} days of time lag. This value is consistent with the *z*DCF and Javelin lags. We assess the lag of this object as rating A.

We had to detrend the light curves of PG 1440+356 before measuring the time lag since the Hα light curve showed a monotonic increase. Without detrending, the CCF values at any lag were higher than 0.4, rendering the lag and its uncertainty measurements unreliable. After detrending, we measured 79^{+68}_{-29} days of time lag. This value is consistent with the *z*DCF and Javelin lags. We note that both the ICCF and *z*DCF are

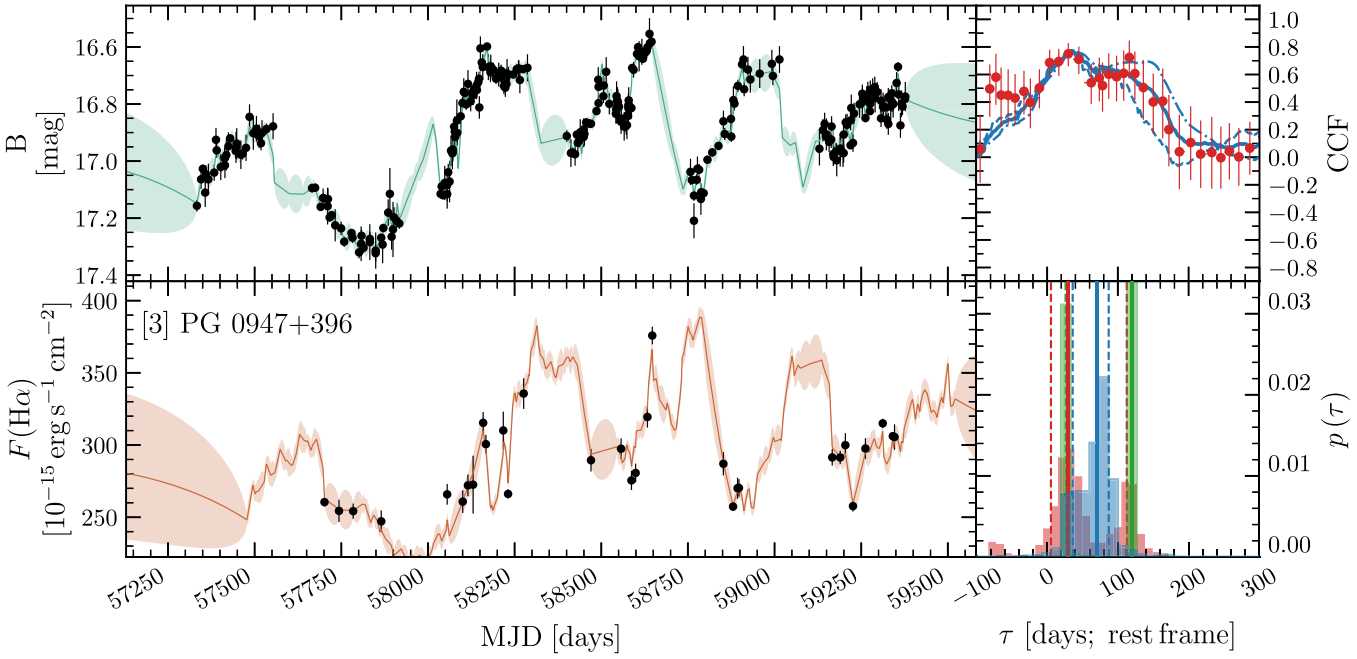

Figure 5. Light curves and time lag measurements of PG 0947+396. The panels are the same as those in Figure 3.

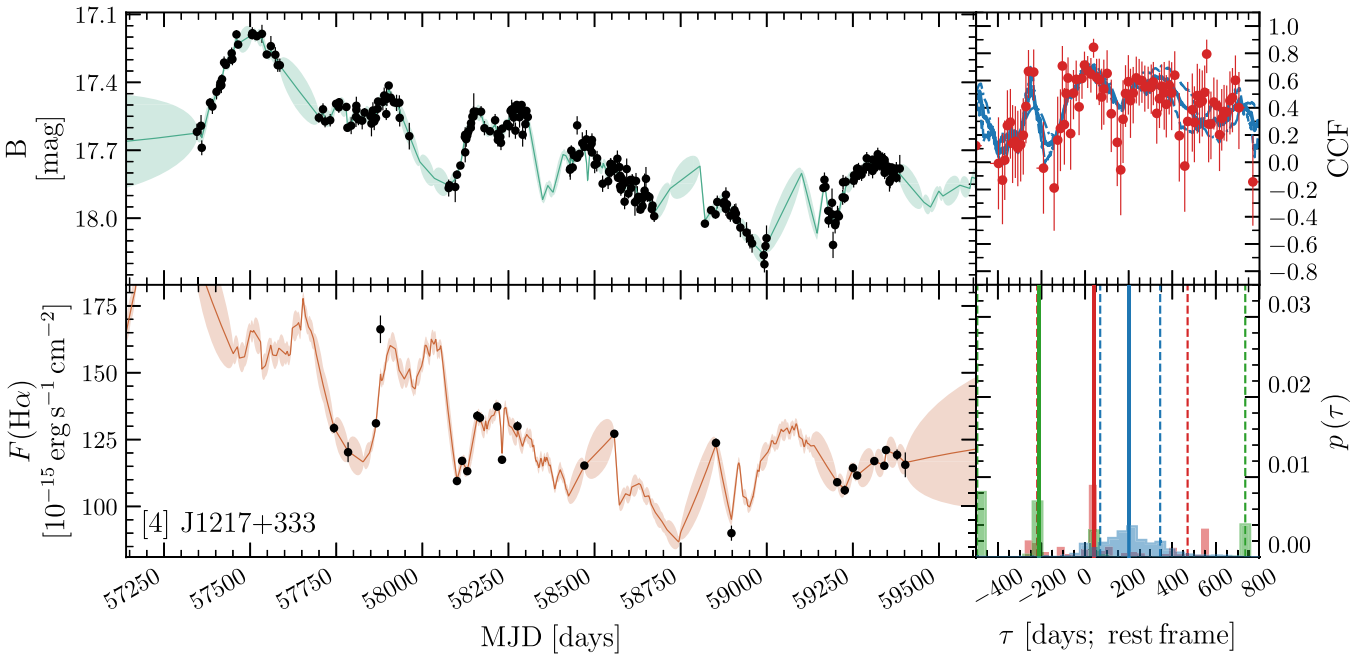

Figure 6. Light curves and time lag measurements of J1217+333. The panels are the same as those in Figure 3.

skewed toward higher lag values, and this is reflected in the measurements. We assess the lag of this object as rating A. We find that the uncertainties of our ICCF-based lag measurements range from 10% to 70%, a considerable portion of which stems from the number of epochs in the light curve. The lack of distinct variability features in the light curve also increases the uncertainty. However, we note that the relative uncertainties of our lag measurements are comparable to those reported in the literature. For example, 95% of the lag measurements we collect in Table 4 have uncertainty between 8% and 70%.

5. The Size–Luminosity Relation

5.1. Determining the Hα BLR Size–Luminosity Relation

To compare the BLR size of Hα with the Hα luminosity, we compiled a sample of Hα lags and luminosities from this work and the literature (Kaspi et al. 2000; Bentz et al. 2010; Barth et al. 2011; Grier et al. 2017; Sergeev et al. 2017; Cho et al. 2020; Feng et al. 2021; Li et al. 2022). While we tried to include as many AGNs as possible, the following objects were excluded. First, Grier et al. (2017) provided quality ratings for

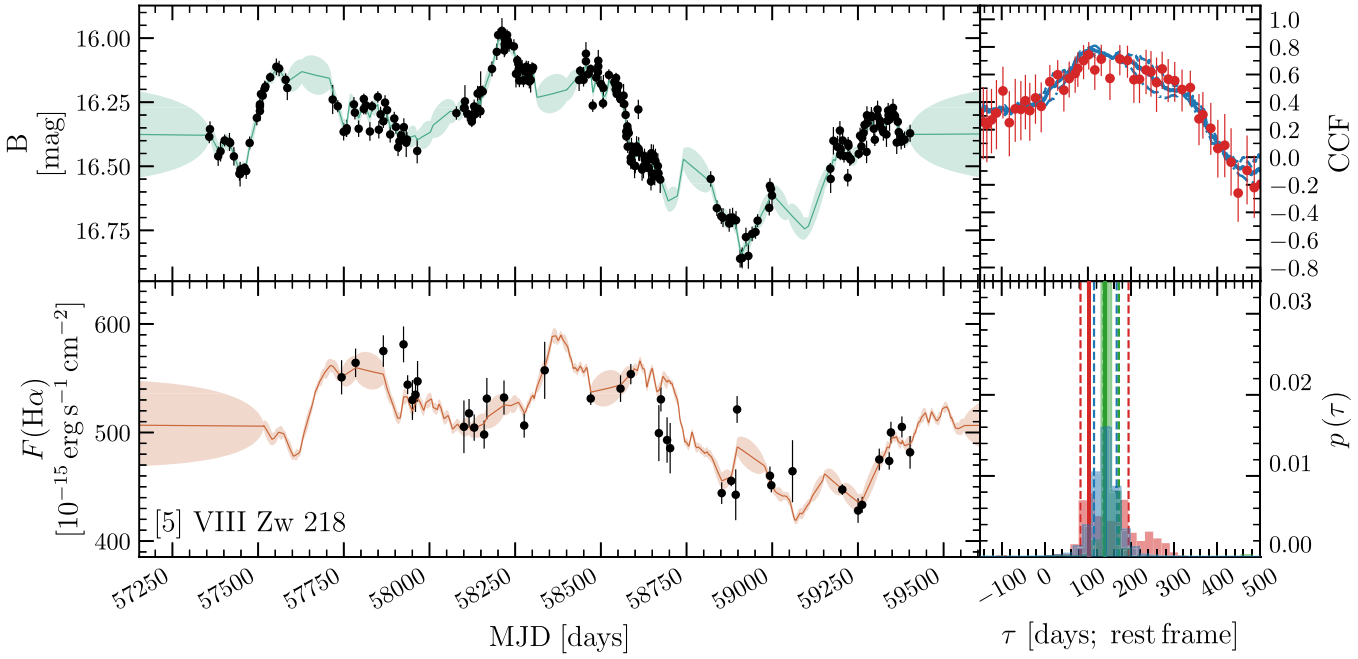

Figure 7. Light curves and time lag measurements of VIII Zw 218. The panels are the same as those in Figure 3.

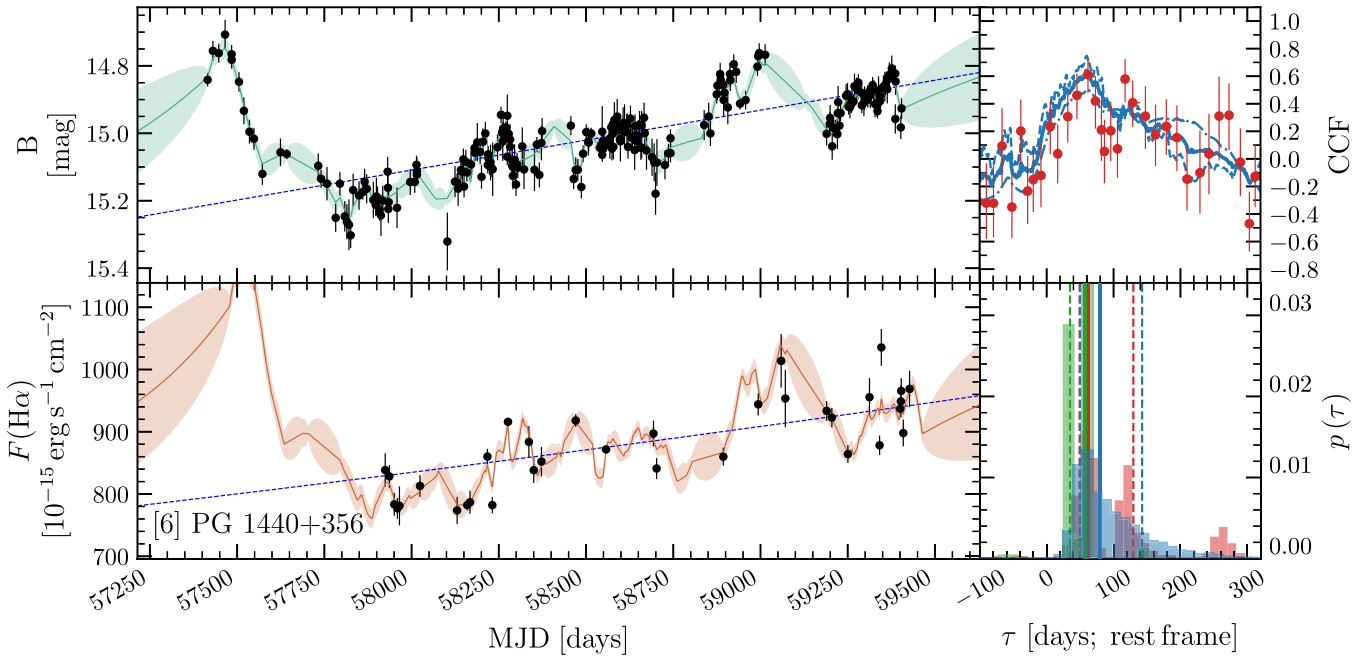

Figure 8. Light curves and time lag measurements of PG 1440+356. The panels are the same as those in Figure 3, except for the left panels, where trend fits for detrending are denoted as blue dashed lines.

time lags, and four objects (out of 18 with Hα lags measured) with ratings of 1 or 2 were excluded. Additionally, we note that the Hα time lags of Ark 564 (Shapovalova et al. 2012) and NGC 7469 (Shapovalova et al. 2017) have been measured. However, the Hα lag of Ark 564 is consistent with zero delay within the error bar, while the CCF between Hα and the continuum light curves of NGC 7469 exhibits multiple peaks with r_{max} values smaller than 0.5. Thus, we did not include these two objects in our analysis. We adopted the time lag values and their 1σ uncertainties from each paper. For the objects presented in this paper, we adopted the ICCF time lag values and their 1σ errors. The lags presented in the observed frame were divided by $1+z$ to convert them into rest-frame lags. We obtained the broad Hα luminosities from the fluxes by multiplying $4\pi {d_L}^2$, where d_L is the luminosity distance. We ignored systematic differences in the methods of measuring flux between the papers, which are discussed in Section 5.2. We also collected the AGN continuum luminosities at 5100 Å for the sample. We applied galactic extinction correction based on the galactic extinction map by Schlafly & Finkbeiner (2011) and the extinction curve by Cardelli et al. (1989). The corrected luminosities, as well as their time lags, are listed in Table 4.

Table 4
The Time Lags and Luminosities

Object	$\log_{10} L_{\mathrm{H}\alpha}$ (erg s^{-1})	$\log_{10} \lambda L_{\lambda}(5100\ \text{Å})$ (erg s^{-1})	$\tau_{\mathrm{H}\alpha}$ (days)	$\tau_{\mathrm{H}\beta}$ (days)	Reference
(1)	(2)	(3)	(4)	(5)	(6)
Mrk 1501	43.15 ± 0.02	44.14 ± 0.02	67^{+24}_{-38}	12^{+8}_{-9}	1
PG 0026+129	43.53 ± 0.04	44.98 ± 0.06	116^{+25}_{-27}	109^{+25}_{-32}	2
PG 0052+251	43.70 ± 0.05	44.92 ± 0.08	183^{+57}_{-38}	86^{+26}_{-27}	2
J0101+422	43.58 ± 0.01	44.89 ± 0.01	118^{+17}_{-17}	76^{+13}_{-12}	1
PG 0804+761	43.72 ± 0.02	44.90 ± 0.08	175^{+18}_{-15}	137^{+24}_{-22}	2
NGC 2617	41.42 ± 0.01	⋯	$6.9^{+1.6}_{-0.8}$	$5.4^{+1.0}_{-1.1}$	6
PG 0844+349	42.98 ± 0.03	44.31 ± 0.04	37^{+15}_{-15}	12^{+13}_{-10}	2
PG 0947+396	43.52 ± 0.02	44.71 ± 0.01	71^{+16}_{-35}	37^{+10}_{-11}	1
Mrk 142	42.08 ± 0.03	43.57 ± 0.04	$2.8^{+1.2}_{-0.9}$	$2.7^{+0.7}_{-0.8}$	3
SBS 1116+583A	41.25 ± 0.03	42.46 ± 0.03	$4.0^{+1.4}_{-1.0}$	$2.3^{+0.6}_{-0.5}$	3
Arp 151	41.52 ± 0.05	42.44 ± 0.05	$7.8^{+1.0}_{-1.0}$	$4.0^{+0.5}_{-0.7}$	3
Mrk 1310	41.34 ± 0.03	42.60 ± 0.03	$4.5^{+0.7}_{-0.6}$	$3.7^{+0.6}_{-0.6}$	3
NGC 4151	41.70 ± 0.02	42.66 ± 0.09	$7.6^{+1.9}_{-2.6}$	$6.2^{+1.4}_{-1.1}$	7
PG 1211+143	43.54 ± 0.05	44.77 ± 0.07	107^{+35}_{-42}	95^{+29}_{-41}	2
Mrk 202	41.13 ± 0.03	42.70 ± 0.02	22^{+1}_{-4}	$3.1^{+1.7}_{-1.1}$	3
NGC 4253	41.62 ± 0.02	42.80 ± 0.02	25^{+1}_{-1}	$6.2^{+1.6}_{-1.2}$	3
NGC 4395	38.45 ± 0.00	39.76 ± 0.01	$0.058^{+0.010}_{-0.010}$	⋯	5
PG 1226+023	44.60 ± 0.03	45.93 ± 0.05	444^{+56}_{-55}	330^{+101}_{-83}	2
PG 1229+204	42.87 ± 0.04	44.07 ± 0.05	67^{+37}_{-43}	34^{+30}_{-17}	2
NGC 4748	41.68 ± 0.03	42.79 ± 0.02	$7.5^{+3.0}_{-4.6}$	$5.5^{+1.6}_{-2.2}$	3
VIII Zw 218	43.29 ± 0.02	44.53 ± 0.01	140^{+26}_{-26}	63^{+16}_{-15}	1
PG 1307+085	43.68 ± 0.04	44.84 ± 0.04	155^{+81}_{-126}	94^{+40}_{-100}	2
PG 1351+640	43.16 ± 0.02	44.73 ± 0.04	227^{+149}_{-72}	⋯	2
SDSS J140812.09+535303.3	41.68 ± 0.04	43.16 ± 0.00	$7.2^{+4.8}_{-5.6}$	$9.0^{+5.6}_{-3.8}$	4
SDSS J140915.70+532721.8	42.27 ± 0.03	43.40 ± 0.00	33^{+14}_{-10}	⋯	4
SDSS J141018.04+532937.5	42.17 ± 0.04	43.56 ± 0.01	23^{+13}_{-8}	14^{+4}_{-6}	4
SDSS J141041.25+531849.0	42.49 ± 0.02	43.79 ± 0.01	12^{+8}_{-7}	11^{+7}_{-7}	4
SDSS J141123.42+521331.7	42.62 ± 0.03	44.12 ± 0.01	13^{+10}_{-14}	$6.5^{+8.8}_{-5.4}$	4
PG 1411+442	43.40 ± 0.02	44.59 ± 0.04	95^{+37}_{-34}	108^{+66}_{-65}	2
SDSS J141151.78+525344.1	42.68 ± 0.06	44.15 ± 0.01	55^{+4}_{-5}	⋯	4
SDSS J141324.28+530527.0	42.44 ± 0.05	43.91 ± 0.00	45^{+14}_{-11}	22^{+11}_{-11}	4
SDSS J141625.71+535438.5	42.71 ± 0.01	43.95 ± 0.00	33^{+19}_{-17}	17^{+6}_{-7}	4
SDSS J141645.15+542540.8	41.85 ± 0.07	43.24 ± 0.01	$9.6^{+4.5}_{-3.0}$	$6.5^{+2.7}_{-1.8}$	4
SDSS J141645.58+534446.8	42.03 ± 0.05	43.64 ± 0.01	18^{+7}_{-8}	$9.7^{+4.0}_{-4.0}$	4
SDSS J141751.14+522311.1	41.97 ± 0.03	42.80 ± 0.01	11^{+6}_{-5}	⋯	4
NGC 5548	42.06 ± 0.03	43.10 ± 0.03	11^{+1}_{-1}	$4.2^{+0.9}_{-1.3}$	3
SDSS J142038.52+532416.5	42.08 ± 0.03	43.46 ± 0.00	20^{+15}_{-15}	27^{+8}_{-14}	4
SDSS J142039.80+520359.7	42.57 ± 0.03	44.10 ± 0.01	18^{+6}_{-16}	$5.1^{+6.4}_{-8.5}$	4
SDSS J142135.90+523138.9	41.96 ± 0.06	43.44 ± 0.00	$7.2^{+3.4}_{-5.6}$	$1.0^{+3.8}_{-4.2}$	4
PG 1426+015	43.40 ± 0.03	44.68 ± 0.07	83^{+42}_{-48}	106^{+45}_{-63}	2
PG 1440+356	43.08 ± 0.03	44.63 ± 0.00	80^{+63}_{-30}	51^{+17}_{-21}	1
PG 1613+658	43.63 ± 0.03	44.95 ± 0.05	38^{+35}_{-19}	39^{+18}_{-20}	2
PG 1617+175	43.24 ± 0.03	44.46 ± 0.08	100^{+28}_{-33}	70^{+27}_{-37}	2
3C 390.3	42.95 ± 0.02	44.02 ± 0.01	153^{+14}_{-14}	84^{+8}_{-8}	8
Zw 229-015	41.47 ± 0.00	42.65 ± 0.05	$5.1^{+0.8}_{-1.1}$	$3.9^{+0.7}_{-0.9}$	9
NGC 6814	41.02 ± 0.03	42.10 ± 0.03	$9.5^{+1.9}_{-1.6}$	$6.6^{+0.9}_{-0.9}$	3
PG 2130+099	43.19 ± 0.03	44.39 ± 0.04	223^{+50}_{-26}	177^{+128}_{-25}	2

Notes. The columns indicate (1) the object identifier, (2) the luminosity of the broad Hα line, (3) the continuum luminosity at 5100 Å, (4) the broad Hα lag, (5) the broad Hβ lag, and (6) the time lag reference. All luminosity values are corrected for galactic extinction based on the extinction value by Schlafly & Finkbeiner (2011) and the extinction curve by Cardelli et al. (1989). The time lag values are presented in the rest frame. The uncertainties shown here are the 68% confidence intervals.
References. (1) This work, with the continuum luminosity and Hβ time lag by J.-H. Woo et al. (2023, in preparation); (2) Kaspi et al. (2000); (3) Bentz et al. (2010), with the continuum luminosity by Bentz et al. (2009) and the host correction by Park et al. (2012); (4) Grier et al. (2017), with the continuum luminosity by Shen et al. (2015); (5) Woo et al. (2019a) and Cho et al. (2020), with the broad Hα luminosity by Cho et al. (2021); (6) Feng et al. (2021); (7) Li et al. (2022); (8) Sergeev et al. (2017); (9) Barth et al. (2011), with the continuum luminosity by Barth et al. (2015).

Table 5
The Best-fit Parameters

x	y	NGC 4395 PG 1226+023	N	K	β	$\sigma_{\rm int}$
(1)	(2)	(3)	(4)	(5)	(6)	(7)
$L_{\rm H\alpha}/10^{42}$ [erg s^{-1}]	$\tau_{\rm H\alpha}/30$ [days]	Included	47	-0.32 ± 0.05	0.61 ± 0.04	0.28 ± 0.03
		Excluded	45	-0.32 ± 0.05	0.58 ± 0.05	0.28 ± 0.03
$\lambda L_\lambda(5100\ \text{Å})/10^{44}$ [erg s^{-1}]	$\tau_{\rm H\alpha}/30$ [days]	Included	46	0.11 ± 0.05	0.58 ± 0.04	0.31 ± 0.03
		Excluded	44	0.12 ± 0.05	0.54 ± 0.06	0.31 ± 0.04
$\lambda L_\lambda(5100\ \text{Å})/10^{44}$ [erg s^{-1}]	$L_{\rm H\alpha}/10^{42}$ [erg s^{-1}]	Included	46	0.71 ± 0.03	0.97 ± 0.03	0.18 ± 0.02
		Excluded	44	0.71 ± 0.03	0.94 ± 0.04	0.19 ± 0.02
$\tau_{\rm H\alpha}/30$ [days]	$\tau_{\rm H\beta}/30$ [days]	PG 1226 only	42	-0.23 ± 0.04	1.01 ± 0.07	0.23 ± 0.03
		Excluded	41	-0.23 ± 0.04	1.00 ± 0.07	0.24 ± 0.03

Notes. The columns indicate (1) the independent variable, (2) the dependent variable, (3) the inclusion of NGC 4395 and PG 1226+023 in the fit, (4) the size of the subset, and (5)–(7) the best-fit parameters to the model described by Equation (2). The best-fit parameters and their uncertainties are given as the median and the standard deviation.

We modeled a generic relation between two variables x and y as

$$\log_{10} y = K + \beta \log_{10} x \pm \sigma_{\rm int} \tag{2}$$

where $\sigma_{\rm int}$ denotes the intrinsic scatter of the relation. To construct the size–luminosity relation of the Hα BLR, we chose y to be $\tau_{\rm H\alpha}/30$ [days], with x being either $L_{\rm H\alpha}/10^{42}$ [erg s^{-1}] or $\lambda L_\lambda(5100\ \text{Å})/10^{44}$ [erg s^{-1}]. Here, variables are normalized to values close to the median of the sample to minimize the posterior correlation of K and β. We fit this relation using the `Python` implementation of the `LINMIX_ERR` algorithm (Kelly 2007).[18] Since this code does not handle different values for upper and lower uncertainties, we took the mean of two uncertainties if both were present. The best-fit parameters are presented in Table 5.

We should note that NGC 4395 has an extremely low luminosity, while PG 1226+023 has an extremely high luminosity compared to other AGNs in our sample. We tested whether removing these outliers from the sample would alter the fit. As presented in Table 5, we found that excluding or including NGC 4395 and PG 1226+023 yields similar best fits, with the largest difference between parameters within the 1σ boundary. Thus, we present the best fit for the size–luminosity relation of the Hα BLR as

$$\log_{10}\left(\frac{\tau_{\rm H\alpha}}{1\,[\rm day]}\right) = (1.16 \pm 0.05) + (0.61 \pm 0.04)\log_{10}\left(\frac{L_{\rm H\alpha}}{10^{42}\ [\rm erg\ s^{-1}]}\right) \tag{3}$$

with $\sigma_{\rm int} = 0.28 \pm 0.03$, and

$$\log_{10}\left(\frac{\tau_{\rm H\alpha}}{1\,[\rm day]}\right) = (1.59 \pm 0.05) + (0.58 \pm 0.04)\log_{10}\left(\frac{\lambda L_\lambda(5100\ \text{Å})}{10^{44}\ [\rm erg\ s^{-1}]}\right) \tag{4}$$

where $\sigma_{\rm int} = 0.31 \pm 0.03$. The best fit, as well as the objects used to derive the fit, is plotted in Figure 9.

[18] https://github.com/jmeyers314/linmix

5.2. Systematic Differences in Luminosities

We note that narrow-line fluxes are handled differently in the literature when measuring the Hα luminosity. For example, in their work, Cho et al. (2021), Feng et al. (2021), and Li et al. (2022) modeled the broad Hα line and narrow-line components separately with multiple Gaussians. Similarly, Grier et al. (2017) modeled the broad line after the narrow lines were modeled and removed using high-pass filtering, which was described by Shen et al. (2016). In contrast, Kaspi et al. (2000), Bentz et al. (2010), Barth et al. (2011), and Sergeev et al. (2017) integrated the flux over certain wavelength windows without removing the narrow lines of Hα, [N II], and even [S II] depending on the object. In principle, direct integration leads to inaccurate measurements by including narrow-line fluxes while excluding the wing of broad Hα. These two effects can work in the opposite way such that they could cancel each other out at a certain level. We assessed that the effect of the Hα wing seems negligible for the objects we included because all aforementioned references chose a sufficiently large interval for direct integration. Moreover, the narrow-line fluxes seem negligible compared to their strong Hα luminosities for the high-luminosity objects that Kaspi et al. (2000) and Sergeev et al. (2017) presented. However, visually inspecting the spectra presented by Bentz et al. (2010) reveals that the Hα fluxes they measured do include a substantial portion of narrow-line fluxes, resulting in a larger scatter.

Measurements of the continuum luminosity suffer from a similar issue. Specifically, Kaspi et al. (2000) and Sergeev et al. (2017) did not remove host galaxy contamination when measuring the continuum flux at 5100 Å. However, the host contamination would be negligible for these high-luminosity AGNs. For instance, Jalan et al. (2023) proposed an empirical correction for host contamination based on the total luminosity at 5100 Å. According to their Equation (2), on average, 30% of the continuum luminosities of 15 AGNs in the aforementioned references can be attributed to their host galaxy starlight. This corresponds to a bias of 0.15 dex, which is far smaller than the intrinsic scatter of our fit. However, we did not use their empirical correction because of its large scatter.

Despite the aforementioned issues, we did not observe any systematic deviation from the size–luminosity relations of the AGNs with inaccurate luminosity measurements. Thus, we conclude that neither the narrow lines nor host contamination induced bias in determining the size–luminosity relation,

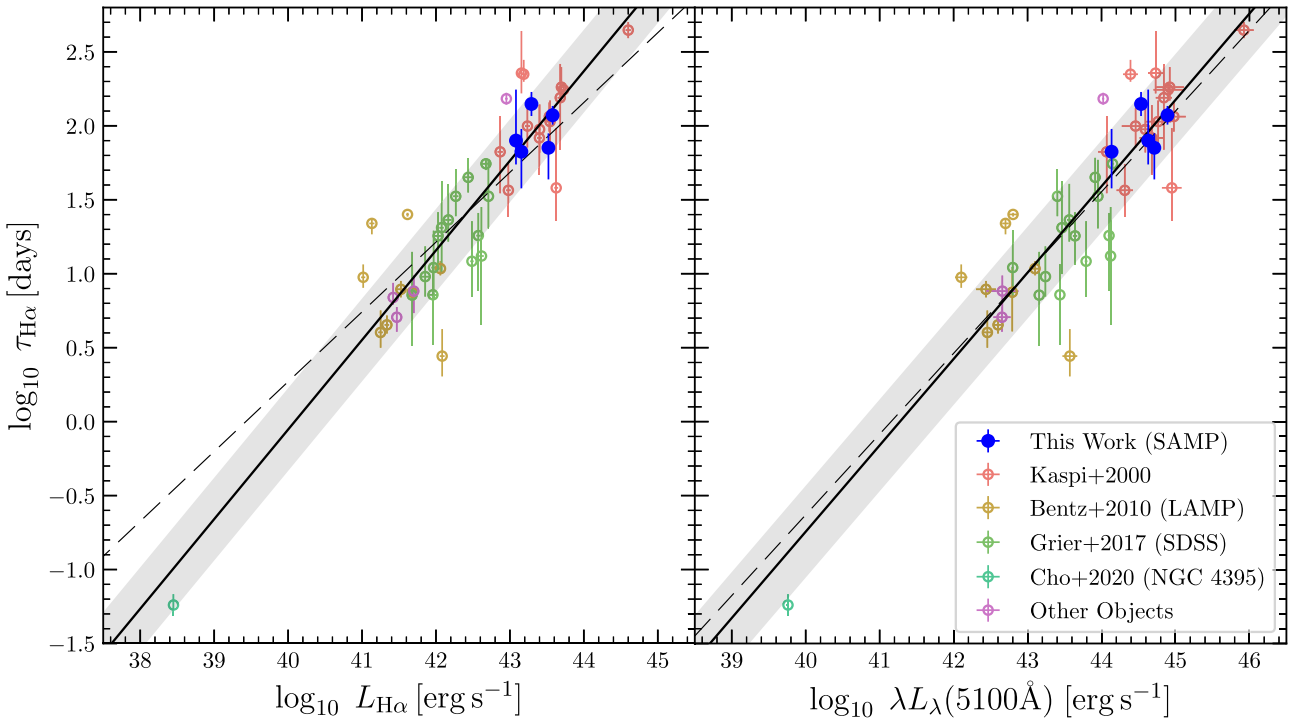

Figure 9. Left: the Hα time lag against the Hα line luminosity. The best-fit relation is denoted with a thick solid line, with the shaded region representing the 1σ intrinsic scatter. The dashed line represents the estimated Hβ lag from the Hα luminosity by combining Equation (1) from Greene & Ho (2005) and Equation (2) from Bentz et al. (2013) with *Clean+ExtCorr* fit parameters (see Section 6.4). Right: the Hα time lag against the continuum luminosity at 5100 Å. The best-fit relation is denoted with a thick solid line, with the shaded area representing the 1σ intrinsic scatter. The dashed line represents the estimated Hβ lag from the continuum luminosity using Equation (2) from Bentz et al. (2013) with *Clean+ExtCorr* fit parameters.

although the intrinsic scatter could be overestimated. For a consistency check, we investigated whether the Hα BLR size–luminosity relation would change by excluding our new measurements. We found that the best-fit slope remained the same and the intrinsic scatter increased slightly (i.e., 0.29 ± 0.03 dex), presumably due to the small size of our new sample. However, the rms scatter of the SAMP AGNs is smaller (0.15 dex) than that of the total sample (i.e., 0.27 dex) as the measurement errors of the SAMP AGNs are much smaller than those of the literature sample. Note that previous Hα lag and error measurements were obtained in various ways. Thus, a uniform analysis of the entire sample is required to better constrain the size–luminosity relation and its scatter.

6. Discussion

6.1. Comparison between the Hα and Continuum Luminosities

The derived size–luminosity relations in Section 5 have slopes very similar to each other, suggesting that the relation between the Hα luminosity and the continuum luminosity at 5100 Å is close to a linear one. Also, theoretically, we expect the Hα emission line flux to scale linearly with the optical continuum luminosity, assuming that all AGNs share the same spectral slope of the power-law continuum (Yee 1980). We directly compare $L_{\rm H\alpha}$ and λL_λ(5100 Å) in Figure 10 by fitting the relation using the generic relation model given by Equation (2). The best-fit parameters are presented in Table 5. The slope $\beta = 0.97 \pm 0.03$ for this relation is virtually the same as unity, and the fit can be simplified as $\lambda L_\lambda(5100\ \text{Å}) = (19 \pm 1) L_{\rm H\alpha}$ with an intrinsic scatter of 0.18 dex. The fit parameter did not change even when we excluded NGC 4395 and PG 1226+023 from the fit, suggesting that a simple linear relation is valid across 7 orders of magnitude of luminosities ($10^{39} < \lambda L_\lambda(5100\ \text{Å})/[\text{erg s}^{-1}] < 10^{46}$, or $10^{38} < L_{\rm H\alpha}/[\text{erg s}^{-1}] < 10^{45}$).

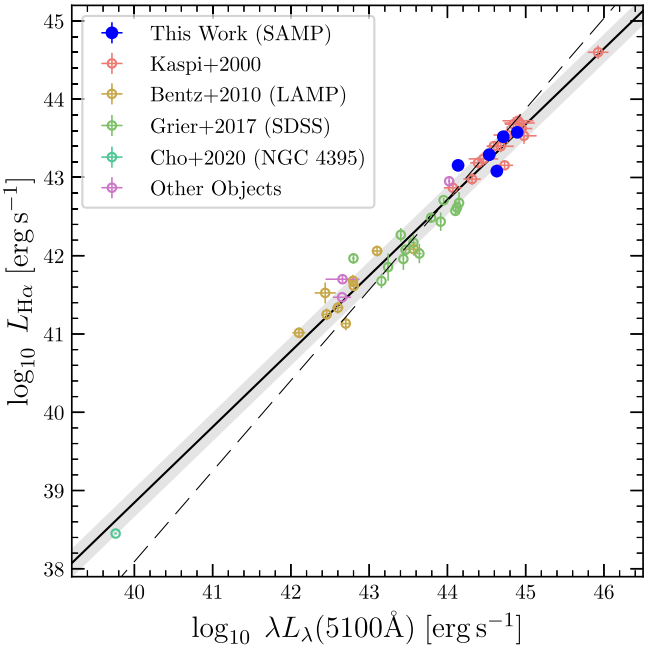

Figure 10. The comparison between the continuum luminosity, λL_λ(5100 Å), and the broad Hα luminosity, $L_{\rm H\alpha}$. The best-fit relation is denoted with a thick solid line, with the shaded area representing the 1σ intrinsic scatter. The dashed line along the diagonal represents Equation (1) from Greene & Ho (2005).

The linearity of this relation contradicts the results by Greene & Ho (2005), who found a supralinear relation between the continuum and line luminosities, with a slope of 1.157 ± 0.005.

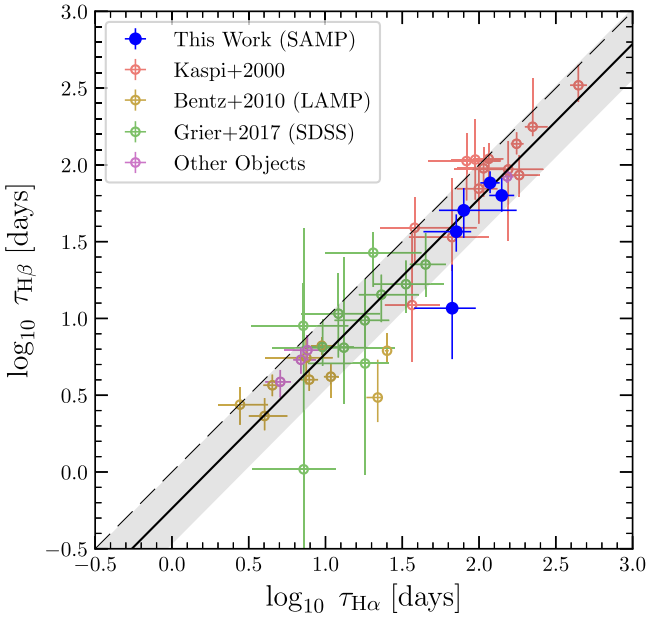

Figure 11. The comparison between the Hα and Hβ lags. The best-fit relation is denoted with a thick solid line, with the shaded area representing the 1σ intrinsic scatter. The dashed line along the diagonal represents the $\tau_{H\alpha} = \tau_{H\beta}$ line.

Note that their sample consists of the AGNs from SDSS, without reverberation mapping results. The major difference from our study is that they did not subtract host galaxy contamination in the continuum luminosity or remove the narrow-line components in measuring the broad Hα luminosity. In the case of narrow-line contamination, Greene & Ho (2005) discussed that the narrow component contribution is only ~7% of the Hα flux, and the slope of the relation did not change even when they used the luminosity of the broad Hα line only. On the other hand, host contamination can systematically change the slope. While continuum subtraction was not performed for some AGNs in Table 4 in our study, these AGNs are mostly high-luminosity objects ($\lambda L_\lambda(5100\ \text{Å}) > 10^{44}$ erg s^{-1}), for which the host galaxy contribution would be negligible. However, Greene & Ho (2005) did not subtract the host galaxy contribution for their sample over the entire luminosity range, including low-luminosity AGNs, where the host galaxy contribution is expected to be systematically larger. While they did exclude galaxies with high host contamination based on modeling the equivalent width of the Ca II K line, the model was constructed from the library of early-type galaxies only, which are not expected to be the host galaxies of low-luminosity AGNs. Presumably these are why we obtained a different slope from that of Greene & Ho (2005). A more recent study by Rakshit et al. (2020), who decomposed SDSS spectra to acquire host-free AGN continuum and broad Hα line luminosities, demonstrated a similar supralinear slope of 1.126 ± 0.004. However, they decomposed the host spectra using eigenspectra constructed from late-type galaxies, which can lead to a similar template mismatch. On the other hand, studies that do not use SDSS spectra deduce slopes close to unity. For example, Shen & Liu (2012) obtained a slope of 1.010 ± 0.042 from 60 objects at $z \sim 1.5$–2.2. Similarly, Jun et al. (2015) demonstrated a slope of 1.044 ± 0.008 with AGNs at $z \sim 0$–6.2 and continuum luminosities within $10^{42} < \lambda L_\lambda(5100\ \text{Å})/[\text{erg s}^{-1}] < 10^{47}$. We discuss that the slope β is unity since (1) all contradicting studies carried out using SDSS spectra had issues with template mismatch, (2) other studies support our results, and (3) a slope of unity predicts the Hα luminosity of NGC 4395 well from its continuum luminosity, while a supralinear slope would underestimate its Hα luminosity.

6.2. BLR Stratification

We now compare the time lag of Hα with that of Hβ. For our five objects, we adopted the Hβ time lags in our previous paper (J.-H. Woo et al. 2023, in preparation). Most of the other objects have Hβ lags measured as well, which are summarized in Table 4. The comparison between the two lags is presented in Figure 11. The best-fit parameters for these two lags are listed in Table 5, which can be summarized as $\tau_{H\alpha} = 1.68\tau_{H\beta}$ with an intrinsic scatter of $\sigma_{\rm int} = 0.23 \pm 0.03$ dex, where the ratio does not depend on the lag. This shows stratified BLRs across a wide range of time lags, which have been predicted and observed before (e.g., Bentz et al. 2010 and references therein), and can be attributed to the optical depth of Hα being larger than that of Hβ.

6.3. Slope of the Size–Luminosity Relation

The slopes of the Hα size–luminosity relation we found in Section 5, 0.61 ± 0.04 and 0.59 ± 0.04, are consistent with those of the Hβ size–continuum luminosity relation by Bentz et al. (2013; 0.55 ± 0.03 with the *Clean+ExtCorr* sample). This is expected since (1) the Hα lags are proportional to the Hβ time lags, as discussed in Section 6.2, and (2) the Hα luminosity is proportional to the continuum luminosity, as discussed in Section 6.1.

While the Hα size–Hα luminosity relation has not previously been reported, some studies have compared the Hβ BLR size with the Hβ luminosity. Wu et al. (2004) obtained the slope of 0.684 ± 0.106 based on available Hβ lags, including those for a large number of objects from Kaspi et al. (2000). A similar slope, 0.687 ± 0.063, was obtained by Kaspi et al. (2005). On the other hand, more recent studies support the Hβ size–Hβ luminosity relation's having a slope close to that of Bentz et al. (2013). For instance, Greene et al. (2010) obtained a much smaller slope of 0.53 ± 0.04. Du et al. (2015) also obtained a smaller slope of 0.51 ± 0.03 with a much larger sample. Our result is broadly consistent with these studies, although further studies are needed to determine the slope of the size–luminosity relation using the broad Hβ luminosity.

6.4. Single-epoch Mass Comparison and Its Implications for IMBH Studies

The mass of the black hole can be estimated by Equation (1). We propose a new single-epoch mass estimator using the luminosity and velocity of broad Hα,

$$\frac{M_\bullet}{10^6 M_\odot} = (13 \pm 1) \times \left(\frac{\sigma_{H\alpha}}{10^3\ \text{km s}^{-1}}\right)^2 \left(\frac{L_{H\alpha}}{10^{42}\ \text{erg s}^{-1}}\right)^{0.61\pm0.04} \quad (5)$$

$$\frac{M_\bullet}{10^6 M_\odot} = (3.2 \pm 0.3) \times \left(\frac{\text{FWHM}_{H\alpha}}{10^3\ \text{km s}^{-1}}\right)^2 \left(\frac{L_{H\alpha}}{10^{42}\ \text{erg s}^{-1}}\right)^{0.61\pm0.04} \quad (6)$$

where we adopt $f = 4.47$ for σ and $f = 1.12$ for the FWHM from Woo et al. (2015).

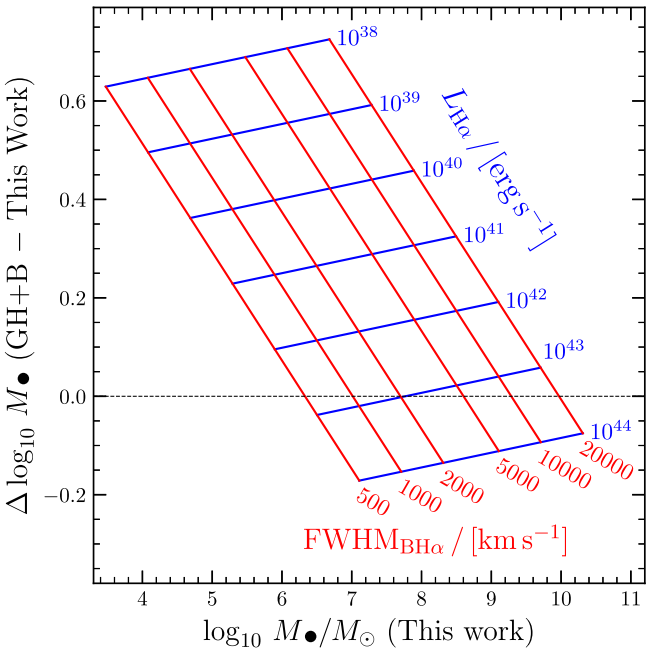

Figure 12. Demonstration of $M_\bullet$ overestimation depending on different parameters. The abscissa represents the single-epoch mass of the black hole estimated from Hα luminosities using the relation we obtained, while the ordinate represents the excess of the mass when estimated using Greene & Ho (2005) and Bentz et al. (2013) as compared to our estimate. The red lines show the contours with the same Hα line widths, while the blue lines show the contours with the same Hα luminosity.

In comparison, Greene & Ho (2005) proposed a method to estimate the size of Hα as follows. The continuum luminosity is first estimated from Hα broad-line luminosities using Equation (1) of their paper. Then, the Hβ size–continuum luminosity relation is used to estimate the Hβ BLR size. A commonly adopted relation is Equation (2) from Bentz et al. (2013) with the parameters obtained using the *Clean+ExtCorr* sample. Combining these yields

$$\log_{10}\left(\frac{\tau_{H\beta}}{1\ [\mathrm{day}]}\right)\quad (\mathrm{Greene\ \&\ Ho}\ +\ \mathrm{Bentz})$$
$$=1.214\ +\ 0.472\log_{10}\left(\frac{L_{H\alpha}}{10^{42}\ [\mathrm{erg\ s^{-1}}]}\right) \qquad (7)$$

which will hereafter be denoted as GH+B. Using this along with Equation (3) in Greene & Ho (2005), one can also construct mass estimates similar to Equations (5) and (6). An example of the analog relation can be found in Reines et al. (2013).

However, the new mass estimator predicts a substantially different mass from the one the GH+B estimator predicts. In Figure 9, the GH+B relation is plotted as a dashed line, and the size–luminosity relation we obtained is plotted as a solid line. While the difference between the two relations is larger than 0.5 dex if $L_{H\alpha} \leqslant 10^{38}$ erg s^{-1}, the Hα size of NGC 4395 is even smaller than what our relation predicts. This difference can be understood as the direct result of the supralinear relation between $L_{H\alpha}$ and λL_λ(5100 Å) by Greene & Ho (2005), as discussed in Section 6.1.

To quantify the difference, we compare our mass estimate with that based on the GH+B relation in Figure 12. While it is negligible for AGNs with masses above $10^9\,M_\odot$, the black hole mass can be overestimated by more than a factor of 2 with the GH+B relation for low-luminosity AGNs with $L_{H\alpha} \leqslant 10^{40}$ erg s^{-1}, which are strong candidates for IMBHs.

IMBHs are important objects because of their relevance to the formation of SMBHs since different scenarios of SMBH formation predict different IMBH mass functions and mass scaling relations even in the local Universe ($M_\bullet$–M_*, $M_\bullet$–σ_*, etc.; e.g., Miller et al. 2015; Greene et al. 2020). In particular, according to the direct collapse scenario, IMBHs at the centers of galaxies have minimum masses of about 10^4–$10^5\,M_\odot$ (e.g., Ferrara et al. 2014).

If our new mass estimator is accurate, the mass measurements of active IMBHs in the literature may have been biased toward larger values. For example, using the GH+B relation, Reines et al. (2013) estimated the masses of AGNs in dwarf galaxies to be in the range of $10^5\,M_\odot$–$10^6\,M_\odot$. However, considering that the Hα luminosities of these AGNs range from 10^{38} erg s^{-1} to $10^{40.5}$ erg s^{-1}, it is possible that the reported masses are overestimated by an average factor of 2–3, with some potentially closer to 30,000 $M_\odot$.

The slope of the Hα-based mass estimator is of critical importance. However, our combined sample does not include any object with 10^{39} erg s^{-1} $< L_{H\alpha} <$ 10^{41} erg s^{-1}, except for one (NGC 4395) with a luminosity smaller than this range. It is necessary to include low-luminosity AGNs, which are more representative of active IMBHs, to properly constrain the slope of the size–luminosity relation and the masses of IMBHs.

Conducting a reverberation mapping campaign for AGNs with Hα luminosities below 10^{41} erg s^{-1} poses substantial challenges. First, these low-luminosity AGNs are expected to exhibit very short Hα lags, requiring intranight monitoring campaigns with a cadence of several hours or even minutes and continuous observations in a several-day time baseline. Such campaigns require the coordination of multiple telescopes. Second, observing these low-luminosity AGNs requires higher sensitivity, which implies the use of larger-aperture telescopes and/or longer exposure times. Despite these difficulties, monitoring campaigns for these low-luminosity AGNs will be crucial to better constraining the Hα S–L relation and to calibrating Hα-based mass estimators, particularly for IMBHs.

7. Conclusions

We present the Hα reverberation mapping results from SAMP. While SAMP mainly aims at performing Hβ reverberation mapping for more than 30 high-luminosity AGNs (J.-H. Woo et al. 2023, in preparation), we additionally obtained time series of Hα spectra for six objects and performed reverberation mapping analysis. By combining our new measurements with the Hα lag measurements of other AGNs in the literature, we investigated the size–luminosity relation of the broad Hα line. Our main results are summarized as follows.

1. We produced Hα light curves based on the spectral modeling of Hα emission lines and measured time lags against B-band continua for six new objects, five of which we consider to be reliable.
2. We collected a sample of AGNs with lag and flux measurements of the broad Hα of 47 AGNs, consisting of our five new objects and 42 from the literature. We calculated the Hα luminosities after correcting for Galactic extinctions.

3. We found the relation between Hα BLR sizes and Hα luminosities to be $\log_{10}\tau_{H\alpha}/1\ \mathrm{day} = (1.16 \pm 0.05) + (0.61 \pm 0.04)\log_{10} L_{H\alpha}/10^{42}\ \mathrm{erg\ s^{-1}}$ and the relation between Hα sizes and 5100 Å continuum luminosities to be $\log_{10}\tau_{H\alpha}/1\ \mathrm{day} = (1.59 \pm 0.05) + (0.58 \pm 0.04)\ \log_{10}\lambda L_{\lambda}(5100\ \text{Å})/10^{44}\ \mathrm{erg\ s^{-1}}$.
4. We found that $\lambda L_{\lambda}(5100\ \text{Å}) = 19\, L_{H\alpha}$, and $\tau_{H\alpha}$:$\tau_{H\beta}$ = 1.68:1.
5. The size–luminosity relation we obtained based on the reverberation mapping results deviates from what is proposed based on single-epoch spectra by Greene & Ho (2005). We demonstrate that for AGNs in the IMBH mass regime, the black hole mass could be substantially overestimated by a factor of 3 on average if the relation by Greene & Ho (2005) is used.
6. We propose two mass estimators based on Hα broad lines assuming $f = 4.47$ for σ and $f = 1.12$ for the FWHM (Woo et al. 2015),

$$\frac{M_\bullet}{10^6 M_\odot} = (13 \pm 1) \times \left(\frac{\sigma_{H\alpha}}{10^3\ \mathrm{km\ s^{-1}}}\right)^2 \left(\frac{L_{H\alpha}}{10^{42}\ \mathrm{erg\ s^{-1}}}\right)^{0.61\pm0.04}$$

$$\frac{M_\bullet}{10^6 M_\odot} = (3.2 \pm 0.3) \times \left(\frac{\mathrm{FWHM}_{H\alpha}}{10^3\ \mathrm{km\ s^{-1}}}\right)^2 \left(\frac{L_{H\alpha}}{10^{42}\ \mathrm{erg\ s^{-1}}}\right)^{0.61\pm0.04}.$$

Acknowledgments

This work has been supported by the Basic Science Research Program through the National Research Foundation of the Korean Government (NRF; 2021R1A2C3008486) and the Samsung Science & Technology Foundation under project No. SSTF-BA1501-05. The work of H.C. was supported by an NRF grant funded by the Korean government (NRF-2018H1A2A1061365, Global Ph.D. Fellowship Program). S. W. acknowledges support from an NRF grant funded by the Korean government (MEST) (No. 2019R1A6A1A10073437). V.N.B. gratefully acknowledges assistance from the National Science Foundation (NSF) Research at Undergraduate Institutions grant AST-1909297. Note that the findings and conclusions do not necessarily represent the views of the NSF. Research at UCLA was supported by the NSF through grant NSF-AST 1907208. Research at UC Irvine was supported by NSF grant AST-1907290. V.U. acknowledges funding support from NASA Astrophysics Data Analysis Program (ADAP) grant 80NSSC20K0450. Support for the program HST-AR-17063.005 was provided by NASA through a grant from the Space Telescope Science Institute, which is operated by the Association of Universities for Research in Astronomy, Incorporated, under NASA contract NAS526555. S.R. acknowledges the partial support of SRG-SERB, DST, New Delhi, through grant No. SRG/2021/001334. We thank the staff of the observatories where data were collected for their assistance.

ORCID iDs

Hojin Cho https://orcid.org/0000-0003-2010-8521
Jong-Hak Woo https://orcid.org/0000-0002-8055-5465
Shu Wang https://orcid.org/0000-0002-2052-6400
Donghoon Son https://orcid.org/0000-0002-4704-3230
Jaejin Shin https://orcid.org/0000-0001-6363-8069
Suvendu Rakshit https://orcid.org/0000-0002-8377-9667
Aaron J. Barth https://orcid.org/0000-0002-3026-0562
Vardha N. Bennert https://orcid.org/0000-0003-2064-0518
Elena Gallo https://orcid.org/0000-0001-5802-6041
Edmund Hodges-Kluck https://orcid.org/0000-0002-2397-206X
Tommaso Treu https://orcid.org/0000-0002-8460-0390
Hyun-Jin Bae https://orcid.org/0000-0001-5134-5517
Wanjin Cho https://orcid.org/0000-0002-4896-770X
Adi Foord https://orcid.org/0000-0002-1616-1701
Yiseul Jeon https://orcid.org/0000-0003-4847-7492
Kyle M. Kabasares https://orcid.org/0000-0003-2632-8875
Wonseok Kang https://orcid.org/0000-0003-3390-1924
Changseok Kim https://orcid.org/0000-0002-2156-4994
Minjin Kim https://orcid.org/0000-0002-3560-0781
Taewoo Kim https://orcid.org/0000-0003-4686-5109
Huynh Anh N. Le https://orcid.org/0000-0003-1270-9802
Matthew A. Malkan https://orcid.org/0000-0001-6919-1237
Daeseong Park https://orcid.org/0000-0001-9877-1732
Hyun-il Sung https://orcid.org/0000-0001-9515-3584
Vivian U https://orcid.org/0000-0002-1912-0024
Peter R. Williams https://orcid.org/0000-0002-4645-6578

References

Alexander, T. 1997, in Astronomical Time Series, ed. D. Maoz, A. Sternberg, & E. M. Leibowitz (Berlin: Springer), 163
Barth, A. J., Bennert, V. N., Canalizo, G., et al. 2015, ApJS, 217, 26
Barth, A. J., Nguyen, M. L., Malkan, M. A., et al. 2011, ApJ, 732, 121
Bentz, M. C., Denney, K. D., Grier, C. J., et al. 2013, ApJ, 767, 149
Bentz, M. C., & Katz, S. 2015, PASP, 127, 67
Bentz, M. C., Walsh, J. L., Barth, A. J., et al. 2009, ApJ, 705, 199
Bentz, M. C., Walsh, J. L., Barth, A. J., et al. 2010, ApJ, 716, 993
Blandford, R. D., & McKee, C. F. 1982, ApJ, 255, 419
Boroson, T. A., & Green, R. F. 1992, ApJS, 80, 109
Cappellari, M. 2017, MNRAS, 466, 798
Cardelli, J. A., Clayton, G. C., & Mathis, J. S. 1989, ApJ, 345, 245
Cho, H., Woo, J.-H., Hodges-Kluck, E., et al. 2020, ApJ, 892, 93
Cho, H., Woo, J.-H., Treu, T., et al. 2021, ApJ, 921, 98
den Brok, M., Seth, A. C., Barth, A. J., et al. 2015, ApJ, 809, 101
Du, P., Hu, C., Lu, K.-X., et al. 2015, ApJ, 806, 22
Event Horizon Telescope Collaboration, Akiyama, K., Alberdi, A., et al. 2019, ApJL, 875, L6
Event Horizon Telescope Collaboration, Akiyama, K., Alberdi, A., et al. 2022, ApJL, 930, L15
Feng, H.-C., Liu, H. T., Bai, J. M., et al. 2021, ApJ, 912, 92
Ferrara, A., Salvadori, S., Yue, B., & Schleicher, D. 2014, MNRAS, 443, 2410
Fisher, R. A. 1921, Metron, 1, 3, https://hdl.handle.net/2440/15169
Flesch, E. W. 2015, PASA, 32, e010
Flesch, E. W. 2021, arXiv:2105.12985
Gravity Collaboration, Sturm, E., Dexter, J., et al. 2018, Natur, 563, 657
Greene, J. E., & Ho, L. C. 2005, ApJ, 630, 122
Greene, J. E., Hood, C. E., Barth, A. J., et al. 2010, ApJ, 723, 409
Greene, J. E., Strader, J., & Ho, L. C. 2020, ARA&A, 58, 257
Grier, C. J., Trump, J. R., Shen, Y., et al. 2017, ApJ, 851, 21
Horne, K. 1986, PASP, 98, 609
Jalan, P., Rakshit, S., Woo, J.-J., Kotilainen, J., & Stalin, C. S. 2023, MNRAS Lett., 521, L11
Jun, H. D., Im, M., Lee, H. M., et al. 2015, ApJ, 806, 109
Kabasares, K. M., Barth, A. J., Buote, D. A., et al. 2022, ApJ, 934, 162
Karamanis, M., & Beutler, F. 2020, arXiv:2002.06212
Karamanis, M., Beutler, F., & Peacock, J. A. 2021, MNRAS, 508, 3589
Kaspi, S., Maoz, D., Netzer, H., et al. 2005, ApJ, 629, 61
Kaspi, S., Smith, P. S., Netzer, H., et al. 2000, ApJ, 533, 631
Kelly, B. C. 2007, ApJ, 665, 1489
Li, S.-S., Feng, H.-C., Liu, H. T., et al. 2022, ApJ, 936, 75

Miller, B. P., Gallo, E., Greene, J. E., et al. 2015, ApJ, 799, 98
NASA/IPAC Extragalactic Database (NED) 2019, NASA/IPAC Extragalactic Database (NED), IPAC, doi:10.26132/NED1
Netzer, H. 1990, in Active Galactic Nuclei, ed. R. D. Blandford et al. (Berlin: Springer), 57
Nguyen, D. D., Seth, A. C., Neumayer, N., et al. 2018, ApJ, 858, 118
Nguyen, D. D., Seth, A. C., Neumayer, N., et al. 2019, ApJ, 872, 104
Oke, J. B. 1990, AJ, 99, 1621
Osterbrock, D. E. 1981, ApJ, 249, 462
Paltani, S., Courvoisier, T. J. L., & Walter, R. 1998, A&A, 340, 47
Park, D., Woo, J.-H., Treu, T., et al. 2012, ApJ, 747, 30
Peebles, P. J. E. 1972, ApJ, 178, 371
Peterson, B. M., Ferrarese, L., Gilbert, K. M., et al. 2004, ApJ, 613, 682
Peterson, B. M., Wanders, I., Horne, K., et al. 1998, PASP, 110, 660
Prochaska, J., Hennawi, J., Westfall, K., et al. 2020a, JOSS, 5, 2308
Prochaska, J. X., Hennawi, J., Cooke, R., et al. 2020b, pypeit/PypeIt: Release 1.0.0, v1.0.0, Zenodo, doi:10.5281/zenodo.3743493
Rakshit, S., Stalin, C. S., & Kotilainen, J. 2020, ApJS, 249, 17
Rakshit, S., Woo, J.-H., Gallo, E., et al. 2019, ApJ, 886, 93
Reines, A. E., Greene, J. E., & Geha, M. 2013, ApJ, 775, 116
Scharwächter, J., McGregor, P. J., Dopita, M. A., & Beck, T. L. 2013, MNRAS, 429, 2315
Schlafly, E. F., & Finkbeiner, D. P. 2011, ApJ, 737, 103
Sergeev, S. G., Nazarov, S. V., & Borman, G. A. 2017, MNRAS, 465, 1898
Shapovalova, A. I., Popović, L. Č, Burenkov, A. N., et al. 2012, ApJS, 202, 10
Shapovalova, A. I., Popović, L. Č., Chavushyan, V. H., et al. 2017, MNRAS, 466, 4759
Shen, Y., Greene, J. E., Ho, L. C., et al. 2015, ApJ, 805, 96
Shen, Y., Horne, K., Grier, C. J., et al. 2016, ApJ, 818, 30
Shen, Y., & Liu, X. 2012, ApJ, 753, 125
Shin, L., Woo, J.-H., Son, D., et al. 2022, AJ, 163, 73
Soldi, S., Türler, M., Paltani, S., et al. 2008, A&A, 486, 411
van der Marel, R. P. 1994, MNRAS, 270, 271
Virtanen, P., Gommers, R., Oliphant, T. E., et al. 2020, NatMe, 17, 261
White, R. J., & Peterson, B. M. 1994, PASP, 106, 879
Woo, J.-H., Cho, H., Gallo, E., et al. 2019a, NatAs, 3, 755
Woo, J.-H., Son, D., Gallo, E., et al. 2019b, JKAS, 52, 109
Woo, J.-H., Yoon, Y., Park, S., Park, D., & Kim, S. C. 2015, ApJ, 801, 38
Wu, X. B., Wang, R., Kong, M. Z., Liu, F. K., & Han, J. L. 2004, A&A, 424, 793
Yee, H. K. C. 1980, ApJ, 241, 894
Zu, Y., Kochanek, C. S., Kozłowski, S., & Peterson, B. M. 2016, ApJ, 819, 122
Zu, Y., Kochanek, C. S., & Peterson, B. M. 2011, ApJ, 735, 80